Reprinted from MONTHLY WEATHER REVIEW, Vol. 121, No. 8, August 1993
American Meteorological Society

Application of the Bratseth Scheme for the Analysis of GALE Data Using a Mesoscale Model

KEITH D. SASHEGYI*

Science Applications International Corporation, McLean, Virginia

DEWEY E. HARMS

Department of Marine, Earth and Atmospheric Sciences, North Carolina State University, Raleigh, North Carolina

RANGARAO V. MADALA

Naval Research Laboratory, Washington, D.C.

SETHU RAMAN

Department of Marine, Earth and Atmospheric Sciences, North Carolina State University, Raleigh, North Carolina

(Manuscript received 14 April 1992, in final form 15 February 1993)

ABSTRACT

The successive correction scheme of Bratseth, which converges to optimum interpolation, is applied for the numerical analysis of data collected during the Genesis of Atlantic Lows Experiment. A first guess for the analysis is provided by a 12-h forecast produced by integrating a limited-area model from a prior coarse operational analysis. Initially, univariate analyses of the mass and wind fields are produced. To achieve the coupling of the mass and wind fields, additional iterations on the geopotential are performed by extrapolating the geopotential to grid points, using improving estimates of the geostrophic wind. This improved geostrophic wind is then used to update the geostrophic component of the initial univariate wind analysis. Use of a background forecast produces much improved mesoscale structures in the analysis. Enhanced gradients of the geopotential and larger wind shears are the result of the coupling of the mass and wind fields, particularly in regions of lower data density. Application of the vertical mode initialization scheme of Bourke and McGregor is used to diagnose the divergent component of the mesoscale circulations produced with the analysis scheme.

1. Introduction

During the 1960s and 1970s, the most widely used objective analysis technique in operational data assimilation and forecast systems was the method of successive corrections. This type of analysis was first introduced by Bergthórsson and Döös (1955), and a number of versions have been developed by Cressman (1959), Barnes (1973), and others. It is still widely used for the analysis of mesoscale systems in the research community (e.g., Koch et al. 1983; Benjamin and Seaman 1985). However, these successive correction schemes possessed a couple of undesirable attributes. First the analysis always converges to the data, which should not be the case when errors exist in the data and the background. Second, observations in regions of high data density are given excessive weight relative to observations in areas of low data density.

In the 1980s, emphasis shifted in the operational community toward the more mathematically complex and computationally expensive method of statistical interpolation, better known as optimal interpolation. With optimal interpolation, analysis errors are minimized with respect to the spatial structure of observational and forecast errors. A concise review of objective analysis can be found in Schlatter (1988). Recently, the method of optimum interpolation has been applied with success to operational limited-area modeling systems (DiMego 1988; Benjamin 1989; Mills and Seaman 1990). In these limited-area forecast systems using optimal interpolation the length scales of the correlation functions are usually reduced from those used with global models to provide more detail at the smaller scales (DiMego 1988).

A paper by Bratseth (1986) has caused a recent resurgence of the successive correction method. He in-

* Current affiliation: Naval Research Laboratory, Washington, D.C.

Corresponding author address: Dr. Keith Sashegyi, Remote Sensing Physics Branch, Code 7220, Naval Research Laboratory, Washington, D.C. 20375-5351.

troduced a successive correction scheme, in which the solution converges toward the solution obtained by optimal interpolation. His technique alleviates the aforementioned shortcomings of previous successive correction methods by using the correlation function for the forecast errors to derive weights that are reduced in regions of higher data density. Additionally, the Bratseth method requires much less computational expense than do optimal interpolation methods. Therefore, it is very attractive for use for a limited-area forecast system when only limited resources are available. This approach to successive correction methodology is currently being used operationally in a multivariate analysis for the limited-area forecast system at the Norwegian Meteorological Institute (Grønås and Midtbø 1987). After a number of iterations of the scheme, the length scale of the correlation functions is further reduced for subsequent iterations to speed the convergence of the scheme at the smaller scales (Grønås and Midtbø 1987; Seaman 1988). A further advantage of reducing the length scale of the correlation function with increasing iteration is that the geostrophic coupling of the geopotential and the wind can be relaxed for the smaller scales (Bratseth 1986). An algorithm similar to the Bratseth scheme has been applied at the U.K. Meteorological Office to directly insert data into both the global and regional models (Lorenc et al. 1991). With each iteration of the U.K. Meteorological Office scheme, the mass and wind variables are updated in a sequential fashion. To maintain balance in their models, changes to the geostrophic component of the wind are derived from any mass changes; the wind changes are nondivergent, and the divergence during integration is damped.

A simplified multivariate, successive correction objective analysis scheme using the Bratseth method has been developed at the U.S. Naval Research Laboratory (NRL) to analyze high-resolution datasets obtained from such field experiments as the Genesis of Atlantic Lows Experiment (GALE), which occurred from 15 January through 15 March 1986. Our scheme also sequentially couples the analyses of mass and wind but in a manner very different from the U.K. Meteorological Office scheme. During the intensive observing periods (IOPs) of GALE, more frequent upper-air soundings were taken at selected National Weather Service sites over the eastern United States, supplemented by additional sites along the coast, dropsondes deployed from aircraft offshore, and a denser set of surface observations (Dirks et al. 1988; Raman and Riordan 1988).

To better use this data, a prior forecast generated by the NRL limited-area weather prediction model is used, as in the operational limited-area models, to provide a first guess for the analysis scheme. The model consists of a fine grid covering the eastern United States and Atlantic offshore, with a resolution of about 55 km, nested inside a coarse grid covering the continental United States and western North Atlantic with a resolution of about 170 km. A prior operational analysis is used to provide the initial conditions for integrating the NRL limited-area model. The analysis covers a similar region as the fine grid but at a lower resolution of 1.5° in latitude and longitude. The analysis grid spacing is consistent with the average upper-air station spacing of about 350 km over the eastern United States. By using such a high-resolution model to generate realistic mesoscale features for the first guess, the resulting analysis should be of a higher resolution than would be possible if a first guess were not used. To remove bad data or data inconsistent with the scales resolved by the numerical model, an efficient quality control procedure was implemented in a manner similar to DiMego (1988).

In this paper, we give a general description of our objective analysis method and provide a qualitative evaluation of the scheme using data from the second IOP of GALE. Results with our new analysis scheme are compared to a Barnes (1973) scheme that was used in the past to enhance large-scale operational analyses (Chang et al. 1989; Shi et al. 1991). The vertical-mode initialization scheme of Bourke and McGregor (1983) is used to diagnose the divergent circulations associated with the analyzed mesoscale features and upper-level jet streaks. The interaction of these secondary circulations in the jet streaks can be important for cyclone development (e.g., Uccellini et al. 1984; Uccellini and Kocin 1987). The impact the new scheme has on these derived mesoscale circulations is tested and compared with the earlier Barnes scheme.

2. The NRL objective analysis scheme

We use a simplified application of the Bratseth scheme compared to the full multivariate implementation used at the Norwegian Meteorological Institute by Grønås and Midtbø (1987). In our scheme, we first perform univariate analyses of the mass and wind fields using the successive correction approach of Bratseth (1986). We analyze for the deviations from a first-guess field, which is derived from a prior 12-h forecast generated by our limited-area model. To provide the coupling between the wind and mass fields, we use the analyzed wind as an initial estimate of the geostrophic wind for a further iteration on the geopotential. The geostrophic wind is used to extrapolate the geopotential to the gridpoint locations, in a fashion similar to Cressman (1959). In each subsequent iteration, an improved geostrophic wind estimate is then defined by the new geopotential gradient, and not by the original wind as was widely used with the Cressman scheme. This change in the geostrophic wind estimate is then used to update the geostrophic component of the initial univariate wind analysis, as in Kistler and McPherson (1975). Further iterations of the wind analysis are performed to enhance the ageostrophic component of the

wind. The initial univariate temperature analysis can then be corrected for the new geopotential thicknesses.

To test the scheme, a set of surface data and upper-air soundings were obtained for the second IOP of GALE from the GALE Data Center (GDC) at Drexel University (Mercer 1987). The data were provided at 10-mb levels from the surface up to 100 mb, and covered a domain over the eastern United States and western North Atlantic from 115° to 45°W and from 10° to 60°N. A higher density of upper-air soundings and surface data is found in the inner GALE region covering the Carolinas and southern Virginia from the Gulf Stream to the Appalachians. The analysis grid covered the data domain with a resolution of 1.5° in latitude and longitude, extending from 116° to 44°W and from 9° to 61.5°N. The initial conditions for the 12 h forecast of our limited-area model are derived from operational analyses obtained at 12-h intervals on a 2.5° hemispheric grid from the National Meteorological Center (NMC). A quality control of the data prior to the analysis is used to remove any data that are inconsistent with this forecast first guess, are not supported by neighboring observations, or are of a scale too small to be resolved by the analysis scheme. In areas without data, such as over the ocean and around the lateral boundaries of the analysis grid, bogus data are derived from the NMC analysis at that analysis time. The analyses are performed on pressure surfaces every 50 mb from 1000 to 100 mb. In a zone along the lateral boundaries of the analysis grid, the analyzed corrections are further merged with corrections to the first guess derived from the NMC analysis. The resulting corrections are bicubically interpolated to the model horizontal fine grid and added to the first guess for display on pressure surfaces. The components of our analysis scheme are

(i) limited-area model forecast,
(ii) data preparation and quality control,
(iii) univariate analysis of the mass and wind field,
(iv) enhancement of the geopotential gradient,
(v) enhancements of the wind field and temperature gradient, and
(vi) boundary values and interpolation to model grid.

We now briefly describe each of these components in turn. More details can be found in the report by Harms et al. (1992).

a. *Limited-area model forecast*

The limited-area model was developed at the Naval Research Laboratory and is detailed in several NRL technical memorandum reports by Madala et al. (1987), Sashegyi and Madala (1990), and Harms et al. (1992). This is a primitive equation model in terrain-following sigma coordinates having a doubly nested grid network. A coarse grid covers a domain including the continental United States from 40° to 140°W and 10° to 70°N, with a horizontal resolution of 2° longitude (170 km at 40°N) × 1.5° latitude (166.5 km). The coarse grid provides the lateral boundary conditions for an inner fine grid, which covers a smaller domain including the eastern half of the United States and extending out over the Gulf Stream from 58° to 102°W and 23.5° to 56.5°N with a finer horizontal resolution of 0.67° longitude (56.7 km at 40°N) × 0.5° latitude (55.5 km). In the vertical, both grids use ten equally spaced sigma levels. Model topography for both grid domains is obtained from the U.S. Navy's 10-min global topographical data. For each model grid point, the average is computed over the grid square with one standard deviation added, and the result smoothed. Climatological mean sea surface temperatures for the month of January of 1° resolution, taken from Reynolds (1982), are interpolated to the model grids. A sea-ice boundary is derived from the U.S. Navy climatological sea-ice boundaries for the months of January and February.

To provide the first guess for the data quality control and analysis we integrate our limited-area forecast model for 12 h starting from a prior NMC analysis. The NMC 2.5° hemispheric analyses are interpolated to the horizontal model grids using Lagrangian cubic polynomial interpolation. The interpolated analyses are then initialized separately on both coarse and fine grids for the first three vertical modes of the numerical model using the vertical mode scheme of Bourke and McGregor (1983), as applied to the NRL model (Sashegyi and Madala 1993). This scheme generates a balanced divergent part of the wind field, while producing only small changes in the geopotential and vorticity. For the coarse grid, lateral boundary values for the model integrations are derived from these initialized NMC analyses by linear interpolating in time.

b. *Data preparation and quality control*

An efficient quality control procedure has been developed for use with the analysis scheme, similar to those at operational weather centers. After checking the upper-air soundings for hydrostatic consistency, we smooth the soundings in the vertical and recompute consistent geopotentials. The temperatures and the u and v wind components are averaged over 20-mb intervals, weighted by the log of pressure for the temperatures and by the mass for the u and v wind components. The humidities, which are more noisy (C. Kreitzberg 1987, personal communication), are smoothed by averaging over 50-mb intervals using the mixing ratios weighted by the mass. Data are retained at 50-mb levels to be more representative of our ten-layer model vertical resolution. For efficiency, the soundings are sorted into 5° latitude–longitude boxes for each pressure level from sea level to 100 mb.

As in the regional analysis at NMC (DiMego 1988),

we perform a "gross" check and a "buddy" check, in which observations with large deviations from the first guess or from neighboring observations are removed. In the gross check, those upper-air observations that differ in magnitude by more than four standard deviations from the first guess are rejected. For sea level pressure a limit of two and a half times the standard deviation is used. Estimates of the standard deviation of the observations from the first-guess forecast are obtained by adding a forecast error growth to the observational error. The values used were slight modifications to those used at operational centers (Dimego 1988; Shaw et al. 1987) and are listed in Table 1. For sea level pressure, an observational error of 1.5 mb is used with forecast error growth of 1.0 mb in 6 h. For the remaining quality control procedures and the analysis, only the deviations of the data from the first guess are retained. As shown by Bratseth (1986), close observations slow the convergence of the iterative scheme. To speed the convergence of the scheme, close observations are replaced by an average "super" observation (superob). To further prevent isolated data from adversely affecting the analysis by aliasing to the larger analysis scales, any remaining isolated observations are also eliminated. In data-sparse regions over the ocean, we use additional bogus soundings, derived from the difference between the first-guess forecast and the NMC 2.5° hemispheric analysis, for the analysis time of interest. To match the resolution of the NMC analysis, we use two bogus soundings spaced 5/3° apart in latitude and longitude in each empty 5° data box in the interior.

c. *Univariate analysis of the mass and wind field*

In the first univariate analysis step, sea level pressure, geopotential, temperature, and humidity corrections to the first guess are successively adjusted at each iteration using the Bratseth (1986) scheme. In this scheme estimates of both the interpolated correction and an observation correction are computed using the iterative formulas. For the geopotential corrections, the interpolated value ϕ_x at the grid point x is given by

$$\phi_x(k+1) = \phi_x(k) + \sum_{j=1}^{n} \alpha_{xj}[\phi_j^o - \phi_j(k)], \quad (1)$$

while the new estimate of the value of the observation correction is given by

$$\phi_i(k+1) = \phi_i(k) + \sum_{j=1}^{n} \alpha_{ij}[\phi_j^o - \phi_j(k)], \quad (2)$$

where ϕ_j^o is the value of the observation, $\phi_x(k)$ and $\phi_j(k)$ are the interpolated values at the grid point and the estimate of the observation value, respectively, for the kth iteration. The sum is over all the n observations. The starting corrections $\phi_x(1)$ and $\phi_j(1)$ are zero. The weights, which are dependent on the covariance of the corrections to the first guess, are in each case given by

TABLE 1. Standard deviation of the observational errors and forecast error growth (in parentheses) for a 6-h forecast period.

Pressure (mb)	Height (m)	Temperature (°C)	Relative humidity (%)	u, v wind (m s^{-1})
1000	5 (8)	1.8 (0.6)	13 (2)	2.5 (1.1)
950	5 (8)	1.8 (0.6)	13 (2)	2.5 (1.1)
900	5 (8)	1.8 (0.5)	13 (2)	2.5 (1.1)
850	6 (8)	1.5 (0.5)	13 (2)	2.5 (1.1)
800	6 (8)	1.5 (0.4)	13 (2)	2.5 (1.1)
750	6 (8)	1.4 (0.3)	12 (2)	2.5 (1.2)
700	6 (8)	1.3 (0.3)	12 (2)	2.5 (1.2)
650	6 (8)	1.2 (0.3)	12 (3)	3.0 (1.3)
600	7 (9)	1.0 (0.3)	12 (3)	3.0 (1.4)
550	8 (10)	1.0 (0.3)	13 (3)	3.0 (1.5)
500	9 (12)	1.0 (0.3)	13 (4)	3.0 (1.6)
450	10 (14)	1.0 (0.4)	13 (4)	3.5 (1.6)
400	12 (16)	1.0 (0.5)	13 (4)	3.5 (1.7)
350	14 (17)	1.0 (0.5)	15 (4)	4.0 (1.7)
300	14 (18)	1.0 (0.6)	17 (4)	4.0 (1.6)
250	14 (18)	1.5 (0.6)	—	4.0 (1.6)
200	15 (18)	1.8 (0.5)	—	4.0 (1.5)
150	18 (18)	1.8 (0.6)	—	4.0 (1.4)
100	20 (17)	2.0 (0.7)	—	3.5 (1.3)

$$\alpha_{xj} = \frac{\overline{\phi_x^t \phi_j^o}}{m_j \sigma^2} = \frac{\rho_{xj}}{m_j} \quad (3)$$

$$\alpha_{ij} = \frac{\overline{\phi_i^t \phi_j^o}}{m_j \sigma^2} = \frac{(\rho_{ij} + \epsilon^2 \delta_{ij})}{m_j}, \quad (4)$$

where the covariances are defined in terms of a correlation function ρ for the true values ϕ^t, ϵ^2 is the ratio of the observation error variance σ_ϵ^2 to the first-guess (forecast) error variance σ^2, and m_j is a "local data density" at the observation location. Here δ_{ij} represents the Kronecker delta function, which is defined to be unity for $i = j$, and zero otherwise. For the forecast error variance, we use the same variance used in the quality control for the variance of the observations from the first-guess forecast (see Table 1). Further, the data density m_i at an observation location is defined by

$$m_i = \frac{1}{\sigma^2} \sum_{j=1}^{n} \overline{\phi_i^o \phi_j^o} = \sum_{j=1}^{n} \rho_{ij} + \epsilon^2. \quad (5)$$

With observation errors included, the estimate of observation is not equal to the analyzed value interpolated to the observation location, but it converges rapidly to the value of the observation itself (Bratseth 1986). However, if there is no observation error, the analyzed value and the observation estimate are both the same value.

We model the correlation function $\rho(r)$ for the geopotential corrections as a Gaussian,

$$\rho(r) = e^{-r^2/d^2}, \quad (6)$$

which is a function of the distance r. The length scale d for the correlation function is defined by 600 km, similar to that used at NMC in the regional model

(DiMego 1988). After the first three or four iterations the length scale is reduced to 330 km for one additional iteration, to speed convergence of the scheme (see also Grønås and Midtbø 1987). After the first pass of our analysis scheme, the data are again checked for inconsistency with the first-pass analysis. Any inconsistent data, which differ by more than 2.5 times (1.5 times for sea level pressure) the standard deviation from the first pass, are removed and the first pass is repeated. The same correlation function is used for the univariate analysis of sea level pressure, temperature, and relative humidity.

For the univariate analysis of wind corrections to the first-guess wind field, different correlation functions are used. The functional form of the correlation functions ρ_u and ρ_v used for the components of the wind field are given by

$$\rho_u = \left[1 - \frac{(y - y_j)^2}{d_u^2}\right]\rho(r) \tag{7}$$

$$\rho_v = \left[1 - \frac{(x - x_j)^2}{d_u^2}\right]\rho(r), \tag{8}$$

where $\rho(r)$ is the correlation function for the geopotential, (x, y) and (x_j, y_j) are the Cartesian positions of an arbitrary point and an observation, respectively, and d_u is a further length scale. The correlation functions for the wind components can be derived from the correlation function $\rho(r)$ for the geopotential, in which case the length scale d_u is given by the length scale d used for $\rho(r)$ (Grønås and Midtbø 1987). Here we have chosen to use the modified length scale d_u of 700 km, which fits the length scale found by Hollingsworth and Lönnberg (1986) where the transverse correlations in the wind reach zero. These correlation functions effectively give smaller weights across the direction of the wind than along it, without having to compute wind direction, as in Benjamin and Seaman (1985). After three to four iterations, the length scales d and d_u are reduced to 330 and 380 km, respectively, for one more iteration to, again, speed convergence.

d. Enhancement of the geopotential gradient

A further four iterations are used for the geopotential correction, using improving estimates of the geostrophic wind at each iteration to extrapolate the geopotential correction to the grid points. An initial estimate of geostrophic wind is obtained from the previous univariate u, v wind corrections by linear interpolation. The interpolated value $\phi_x(k+1)$ at the grid point is now given after the kth iteration by

$$\phi_x(k+1) = \phi_x(k) + \sum_{j=1}^{n} \alpha_{xj}\{\phi_j^o - \phi_j(k) - c_j(y - y_j)f_j[u_{g,j}(k) - u_{g,j}(k-1)] + c_j(x - x_j)f_j[v_{g,j}(k) - v_{g,j}(k-1)]\}, \tag{9}$$

and the observation estimate $\phi_i(k+1)$ is

$$\phi_i(k+1) = \phi_i(k) + \sum_{j=1}^{n} \alpha_{ij}\{\phi_j^o - \phi_j(k) - c_j(y_i - y_j)f_j[u_{g,j}(k) - u_{g,j}(k-1)] + c_j(x_i - x_j)f_j[v_{g,j}(k) - v_{g,j}(k-1)]\}, \tag{10}$$

where ϕ_j^o is the value of the observation, $\phi_j(k)$ is the observation estimate, and $u_{g,j}(k)$ and $v_{g,j}(k)$ are estimates of the geostrophic wind correction at the observation point for the kth iteration. Here $u_{g,j}(k-1)$ and $v_{g,j}(k-1)$ are the prior estimates of the value of the geostrophic wind at the observation point. In the above, f is the Coriolis parameter and c is a geostrophy factor that reduces to zero near the equator. For the next iteration, an improved estimate of the geostrophic wind correction is computed at the grid points from the new interpolated values of the geopotential given by Eq. (9). Values $u_{g,j}(k+1)$ and $v_{g,j}(k+1)$ of the geostrophic wind at the observation point are then computed by linear interpolation. For the four iterations a single correlation scale d of 600 km is used. In this way, we correct the larger scales only, without changing the smaller scales that are not as geostrophic.

In computing the new estimates of the geostrophic wind components $u_{g,x}$, $v_{g,x}$ from the new geopotential ϕ_x at the grid points, the same geostrophy factor c and a modified Coriolis parameter f^* are used, where

$$u_{g,x} = -\frac{c}{f^*}\frac{\partial \phi_x}{\partial y} \tag{11}$$

$$v_{g,x} = \frac{c}{f^*}\frac{\partial \phi_x}{\partial x}. \tag{12}$$

The geostrophy factor c depends on the latitude θ in degrees as

$$c = \begin{cases} 1, & \text{for } |\theta| > 30^\circ \\ 0.5(1 + \cos 12\theta), & \text{for } 15^\circ \leq |\theta| \leq 30^\circ \\ 0, & \text{for } |\theta| < 15^\circ, \end{cases} \tag{13}$$

and f^* only differs from f in a 15° latitude band around the equator where its magnitude is given by that at 15°N, and it has the same sign as f.

e. Enhancements to the wind and temperature gradients

Following Kistler and McPherson (1975), we adjust the geostrophic part of the corrections to the wind field to match the new corrections for the geopotential. That is, the univariate wind corrections are modified by adding the difference in the geostrophic wind between the enhanced and univariate analysis of the geopotential. In this way the enhanced horizontal shear of the geostrophic wind is preserved in the wind analysis. A further four univariate passes of the wind analysis are then performed to improve the corrections for the ageostrophic component of the wind. After the corrections have been computed at all pressure levels of the analysis, the univariate temperature corrections are adjusted to match the computed thickness corrections.

f. Boundary values and interpolation to model grid

In a nine-point zone along the lateral boundaries of our analysis grid, we merge the analyzed corrections with values interpolated from the NMC analysis. The analyzed corrections in the first six points closest to the boundary are replaced by the NMC values, while a linear weighting of (0.25, 0.75), (0.5, 0.5), (0.75, 0.25) is used to merge the next three interior analyzed values with the NMC values. The final corrections are then bicubically interpolated to the horizontal fine grid of the model and added to the first guess for display of the final analysis on pressure surfaces.

For use on the forecast model grid, the analysis corrections are also interpolated to the sigma levels of the model. An initial estimate of new surface pressure is first computed from the analyzed full fields on the pressure levels. The surface pressure of the background forecast is similarly computed from the temperature and height on the pressure levels. The difference in surface pressure between the two is then added to the original surface pressure of the background forecast to obtain the corrected surface pressure. The analysis deviations are then linearly interpolated in the vertical to the model sigma levels and added to the first-guess model forecast. The thermodynamic variables (temperature and humidity) are interpolated to the model sigma levels, assuming they are linear in log of pressure, while wind components are interpolated assuming they are linear in pressure. A balanced divergent part of the wind can then be obtained by applying the initialization procedure described in Sashegyi and Madala (1993).

3. Testing the analysis scheme

Analyses were made with the new scheme using the surface and atmospheric sounding data collected during IOP 2 of GALE for the period 0000 UTC 23 January to 1200 UTC 28 January 1986. During this period, cold-air damming occurred east of the Appalachians and a coastal front developed along the east coast of the United States, followed by cyclone development off Cape Hatteras. This range of mesoscale and synoptic-scale features occurred in the region of data coverage and provided an ideal test of the new scheme. The mesoscale features produced with the new scheme could also be compared to the mesoscale analyses of this period by Bosart (1988) and Doyle and Warner (1990). The NMC hemispheric analyses will provide a comparison for the synoptic-scale features produced with our new scheme. The impact of the different components of our new scheme are demonstrated using the analysis for 1200 UTC January 25. The effect of

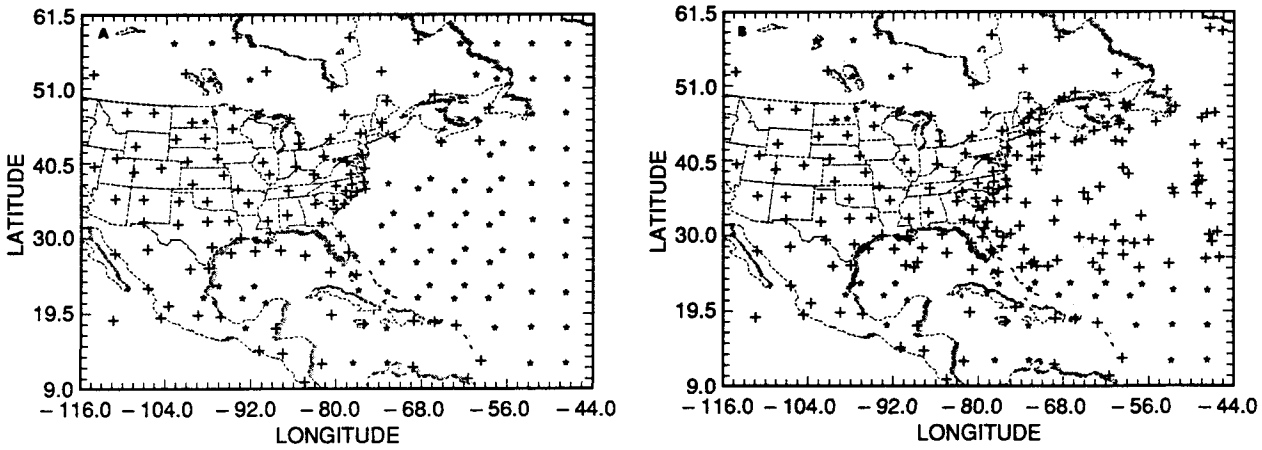

FIG. 1. The location of the data after quality control at 1200 UTC 25 January for (a) the geopotential height at 500 mb and (b) the sea level pressure. The observations are indicated by the plus sign, while bogus values are indicated by the asterisk. The analysis grid is indicated by the tick marks along the domain boundary.

reducing the width of the correlation function and of using superobs is also tested.

For 1200 UTC January 25, the locations of the data that remain after the quality control are shown in Fig. 1 on the domain of the analysis grid. The locations of the observations are shown by the crosses, while the stars show the NMC bogus data, which have been added in data-sparse regions. The analysis grid is indicated by the small tick marks every 1.5° along the latitude and longitude axes. With the 500-mb geopotential height data, few superobs were required but many NMC bogus soundings were added over the ocean. With the sea level pressure data, many more observations were available, many of which have been averaged and replaced by superobs.

To provide a fair comparison on the synoptic scales at the same resolution as our new analysis scheme, the NMC 2.5° hemispheric analyses are themselves enhanced by applying the Barnes (1973) scheme we have used in Chang et al. (1989) to this GALE data. In this application of the Barnes (1973) scheme, a two-step correction of the deviations of the GALE data from the NMC hemispheric analyses are performed using Gaussian weighting defined according to the criterion of Koch et al. (1983). Using an average spacing for the upper-air data over the eastern United States of 350 km, the criterion gives a length scale [d in Eq. (6)] of about 500 km for the Gaussian weighting function for the first pass and 275 km for the second pass. As in Shi et al. (1991), the same quality control described in section 2b is also applied here to the data using the standard deviation of the observational errors listed in Table 1. The first pass for this enhancement of the NMC fields is performed here on the same grid as the new analysis. However due to the decreasing data density outside the region of the eastern United States, the second pass of the Barnes scheme must be limited to a smaller domain, if aliasing is not to occur. The region for the second pass is bounded by longitudes 108°, 68°W and latitudes 25.5°, 49.5°N for the upper-air data, and 22.5°, 49.5°N for the sea level pressure data. A linear weighting is then used to merge the first and second passes over four more analysis grid points inside the second-pass domain. In contrast, this restriction is not necessary with the Bratseth scheme, which adjusts the weights for the changing data density over the whole analysis domain. The synoptic situation during GALE IOP 2 is now described using these enhanced NMC analyses.

a. Description of the synoptic situation

Riordan (1990) and Doyle and Warner (1990) describe in detail the development of the coastal front during GALE IOP 2. With the movement of a cold front off the east coast of the United States at 1200 UTC 23 January, a wedge of cold air is formed behind the front between the Appalachian Mountains and the coast in the next 24 h. The temperature gradient across the coastline is enhanced by the strong sensible heating of the air over the Gulf Stream (Warner et al. 1990). In the subsequent onshore easterly flow behind the cold front, a coastal front develops offshore along the Carolina coast, and by 1200 UTC on 25 January, a 1000-km-long coastal front paralleled the coastline. The easterly flow regime can be seen in the enhanced NMC analysis for 1000 mb shown in Fig. 2a on the model's horizontal fine grid. The enhanced NMC analysis is, however, unable to resolve the strong thermal gradient along the coast. In the upper levels of the atmosphere, a broad, long-wave trough was present over the central United States at this time (Fig. 2b). During the next 24 h, the trough moved eastward and deepened rapidly due to a second short-wave digging southward in the long-wave trough. By 0000 UTC 26 January, the coastal front extended from Georgia to southern New England and a weak low moved up the coast along the front, reaching the Chesapeake Bay by 1200 UTC 26 January (Fig. 2c). In the next 12 h the coastal low merges with a weak trough, seen in Fig. 2c, moving eastward from the Great Lakes.

The disturbance that ultimately became the first of the major cyclones of GALE was present (Fig. 2a) as a minor frontal wave in extreme southeast Texas at 1200 UTC 25 January. Aloft a major short wave was digging southeastward in the long-wave trough. The surface disturbance remained weak as it advanced along the Gulf coast, and on 26 January the surface wave weakened further as it moved across Georgia. In response to the strong upper-level short wave reaching the East Coast, a new center formed off Cape Hatteras, which deepened rapidly as it moved north, as it combined with the preexisting waves associated with the northward-moving coastal low and eastward-moving trough. By 1200 UTC 27 January, the well-developed low pressure center can be seen (Fig. 2d) crossing the New England coast.

b. Impact of the new scheme

We demonstrate the impact of each of the components of our new analysis scheme with the analysis for 1200 UTC 25 January. The first-guess for the analysis is generated by a 12-h forecast with our limited-area model, where the initial conditions are derived from the NMC 2.5° hemispheric analysis for 0000 UTC 25 January 1986. The resulting first guess is illustrated in Fig. 3, which shows the sea level pressure, 1000-mb winds and temperature, and the 500-mb prediction of height, wind, and temperature on the model's horizontal fine grid. The model has produced a strong wedge of cold air and strong ridging east of the Appalachians (Fig. 3a). The strong temperature gradient along the Carolina coast in the region of strong onshore flow shows conditions favorable for the development of a coastal front. The 1200 UTC 25 January analysis

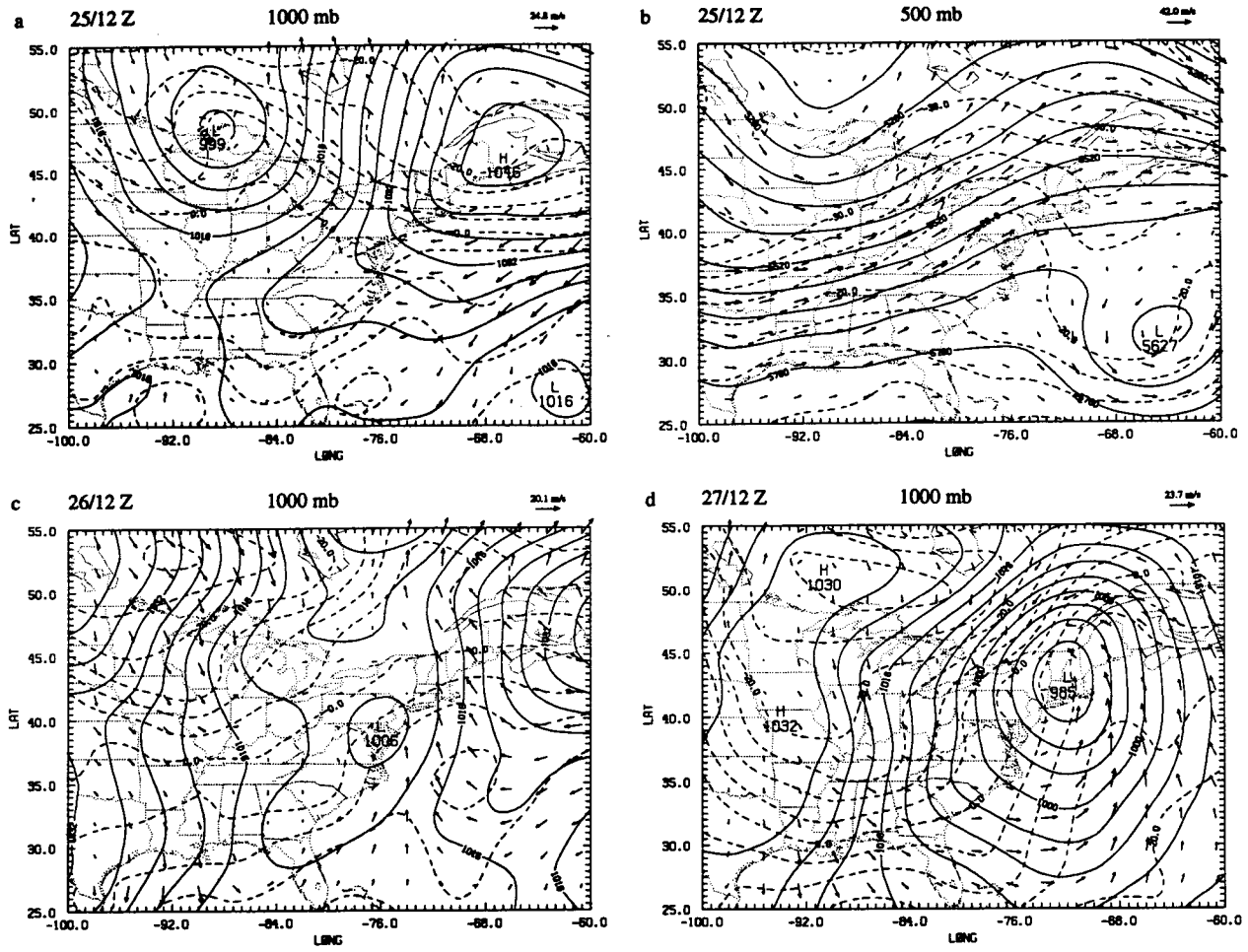

FIG. 2. (a) Sea level pressure (mb), temperature (°C), and winds at 1000 mb, and (b) geopotential height (gpm), temperature (°C), and winds at 500 mb for the enhanced NMC analysis for 1200 UTC 25 January. Here (c) and (d) are as in (a) except for 1200 UTC 26 and 27 January, respectively. Contours of sea level pressure are 4 mb and 5°C for temperature at 1000 mb. At 500 mb, contours are 60 gpm for geopotential and 2.5°C for temperature. Maximum wind vectors indicated by labeled arrow in meters per second. Model horizontal grid indicated by small tick marks along axes.

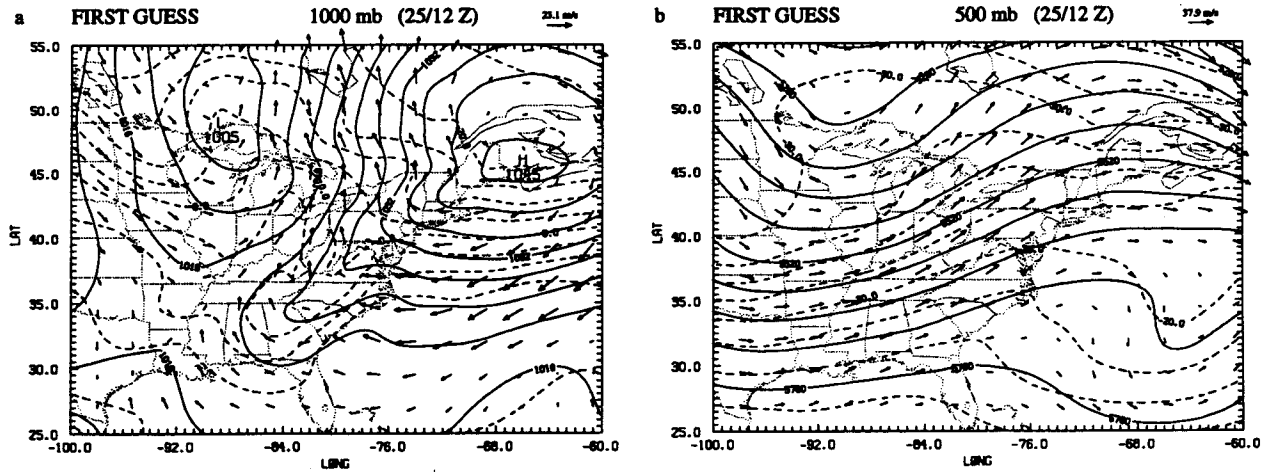

FIG. 3. The first guess at 1200 UTC 25 January for (a) sea level pressure (mb), 1000-mb temperature (°C), and winds; and for (b) geopotential height (gpm), temperature (°C), and winds at 500 mb. Contours as in Fig. 2.

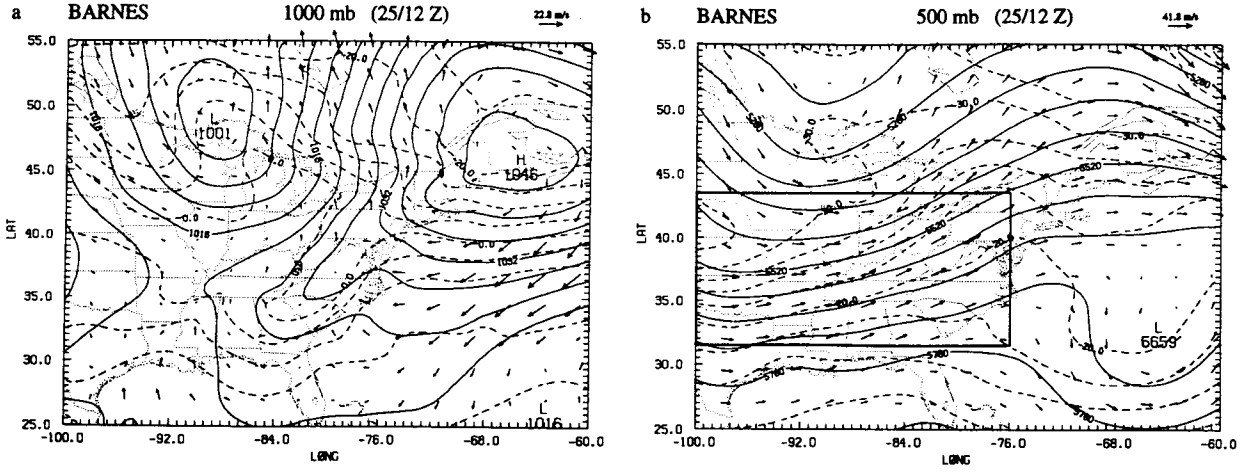

FIG. 4. The Barnes analysis at 1200 UTC 25 January for (a) sea level pressure (mb), 1000-mb temperature (°C), and winds; and for (b) geopotential height (gpm), temperature (°C), and winds at 500 mb. Contours as in Fig. 2.

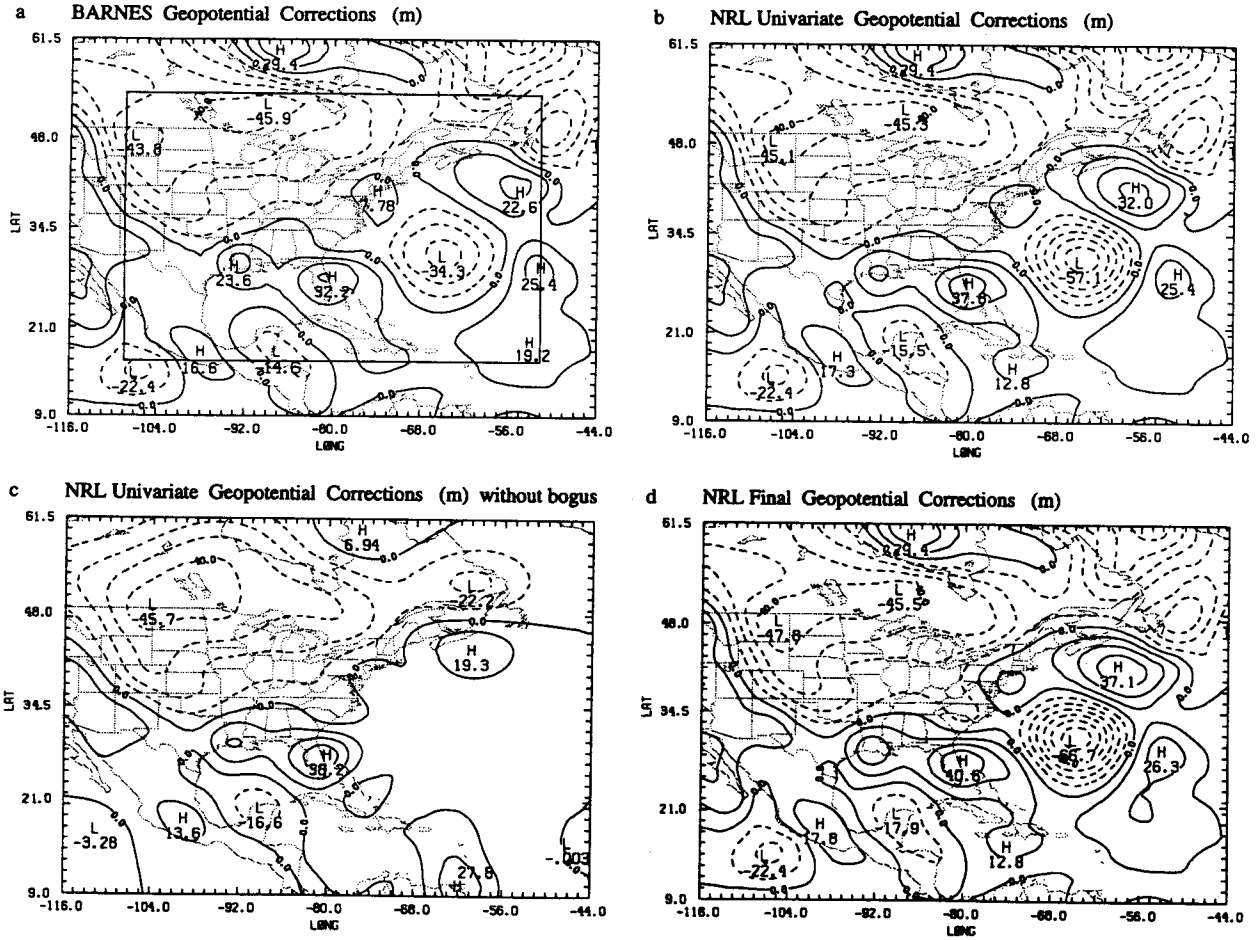

FIG. 5. The geopotential height corrections (gpm) at 500 mb for 1200 UTC 25 January with (a) the Barnes scheme, (b) the NRL univariate analysis, (c) the NRL univariate analysis without bogus data, and (d) the NRL multivariate analysis. Contours of geopotential orrections are every 10 gpm. Analysis grid points indicated by the tick marks along the axes.

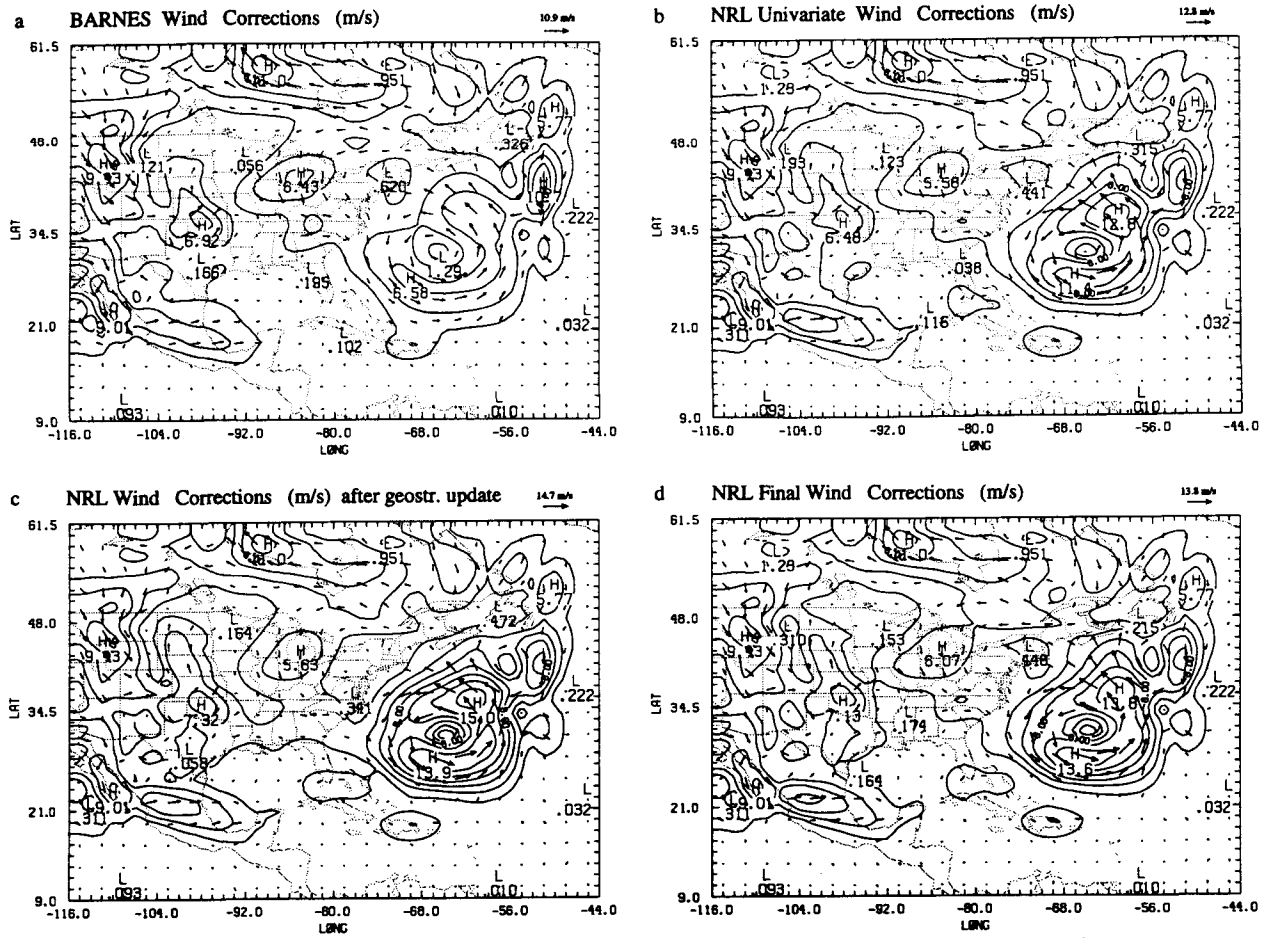

FIG. 6. The wind corrections ($m\ s^{-1}$) at 500 mb for 1200 UTC 25 January with (a) the Barnes scheme, (b) the NRL univariate analysis, (c) the NRL analysis after updating the geostrophic wind, and (d) the NRL multivariate analysis. Contours of wind speed corrections are every 2 $m\ s^{-1}$.

of Doyle and Warner (1990) verifies that the cold-air damming and coastal front with the strong onshore flow were indeed present (see Fig. 2b of Doyle and Warner). This tight thermal gradient along the coast could not be resolved in our enhanced NMC analysis shown in Fig. 2a. However, the low of 1005 mb over Lake Superior is too weak in the first guess (Fig. 3a) when compared to the enhanced NMC analysis (Fig. 2a). Aloft at 500 mb, the long-wave trough over the eastern United States in Fig. 3b is also too weak, and model forecast has failed to produce the cutoff low over the western Atlantic, which can be seen in the enhanced NMC analysis in Fig. 2b. The cutoff low in the enhanced NMC analysis is about 70 m deeper than the weak trough present in the first guess.

The improvement achieved alone by using a model-generated background field is first illustrated by repeating the Barnes analysis (which was used earlier for the enhancement of the NMC hemispheric analysis) using the aforementioned 12-h model forecast as the background field. The resulting Barnes analysis for 1000 and 500 mb is shown in Fig. 4. The surface low over Lake Superior is corrected to within a millibar in Fig. 4a, and the cold-air damming and strong temperature gradient from the first guess are retained. Aloft at 500 mb, both the long-wave trough and the low off the coast have been correctly deepened in Fig. 4b. We can also see that the −30°C temperature contour has been shifted eastward in closer agreement with the enhanced NMC analysis in Fig. 2b. Therefore, in the region over the eastern United States, where there is a large amount of data, the Barnes scheme using the limited-area model forecast as a first guess, is able to produce a good synoptic-scale analysis and retain the mesoscale cold wedge and tight temperature gradient along the coast from the first guess. But the cutoff low over the western Atlantic in the Barnes analysis is still too weak by some 32 m when compared to the enhanced NMC analysis. However, the cutoff low does lie outside of the region influenced by the second pass of the

Barnes scheme (see beginning of section 3). The region fully updated by the second pass is shown by the solid rectangle inside Fig. 4b.

In Figs. 5 and 6, we compare the analysis corrections for the 500-mb geopotential height and winds after each of the remaining components of the new analysis scheme with that produced by the Barnes scheme. The figures show the entire region of the analysis grid, with the analysis grid points indicated by the small tick marks along the axes. The geopotential and wind corrections to the first guess obtained with the Barnes scheme are shown in Figs. 5a and 6a. The six-point region around the boundary, where analyzed values are replaced with values interpolated from the NMC 2.5° hemispheric analysis, is indicated by the solid rectangle in Fig. 5a (see section 2f). The deepening of the long-wave trough and a strong cutoff low are readily apparent in the geopotential height corrections in Fig. 5a. The winds around the cutoff low are strengthened in Fig. 6a, and an ageostrophic flow south of the Great Lakes is produced. In Figs. 5b and 6b we compare the result after the initial univariate analysis of the geopotential height and wind is carried out with the new analysis scheme as described in section 2c. The only change is that the Bratseth scheme is used for the analysis instead of the Barnes scheme. In the data-rich area over the eastern United States, only small differences are found in the 500-mb geopotential height and wind corrections. The maximum in the ageostrophic flow south of the Great Lakes is somewhat weaker with the Bratseth scheme. Over the western Atlantic, the cutoff low is much deeper when using the Bratseth scheme, which is able to adjust the weights for the changing data density and can be applied without restriction over the whole analysis domain. The influence of the bogus data used in the analysis can be seen in Fig. 5c, which shows the 500-mb geopotential corrections produced when no bogus data are used with the Bratseth scheme. The bogus data clearly define the cutoff low over the western Atlantic in Fig. 5b, providing a good check of our scheme.

The impact of using the wind information to extrapolate the geopotential heights in the second stage of the new scheme (section 2d) is demonstrated in Fig. 5d. The cutoff low is seen to be further deepened. The long-wave trough over the central United States is also deepened somewhat and heights are lowered over the Carolinas. After updating the geostrophic component of the wind field for the new geopotential height corrections (section 2e), we see the winds around the cutoff low in Fig. 6c are also strengthened with a stronger wind shear to the south of the low center. With the enhancement of the ageostrophic flow in the final stage of the scheme (section 2e), the intensity of the wind maxima around the south and western sides of the cutoff low have been reduced in Fig. 6d, but the wind shear is maintained. The reduction in the peak winds is not surprising, since the geostrophic wind is an overestimate of the actual wind in a low. The ageostrophic flow from the Great Lakes to the coast has also been strengthened somewhat.

c. *Convergence of the new scheme*

We illustrate in Fig. 7 the rate of convergence of the Bratseth (1986) scheme for our case with a fixed correlation length scale of 600 km for the univariate analysis of the 500-mb geopotential height at 1200 UTC 25 January. The curves in the figure show the root-mean-square (rms) errors for both the analyzed values and the observation estimates (computed here as differences from the observation values), as a function of the iteration number. With increasing iteration, the observation estimate rapidly approaches the value of the observation, while the analyzed value rapidly converges to a value different from the observation but the same as that which would be produced by optimum interpolation (Bratseth 1986). As described in section 2c, the length scale of the correlation function is reduced to 330 km after just four iterations in our case to speed the convergence of the scheme. A large decrease results in the magnitude of the rms errors for both the analyzed value and observation estimate of the 500-mb geopotential, as shown by the crosses in Fig. 7. The rms error for the analyzed values is then within 5% of the optimum value that is produced after 100 iterations with a fixed length scale. The differences between the analyzed fields produced in either case are small.

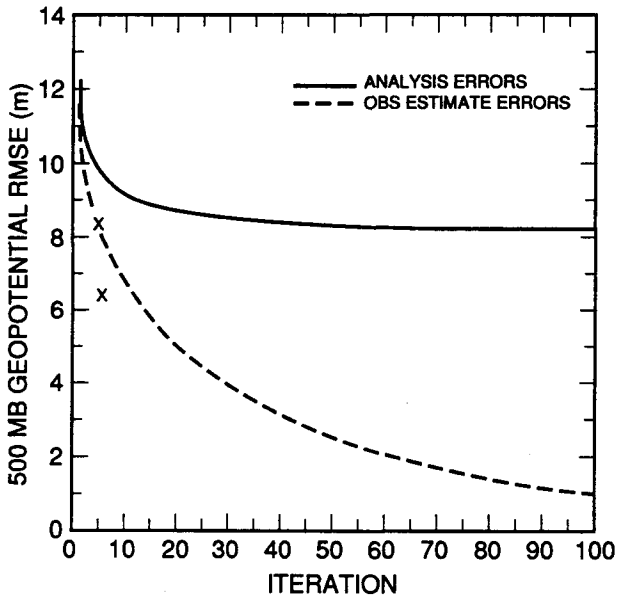

FIG. 7. The rms errors for the analyzed values [derived from Eq. (1)] at the observation locations (solid curve) and for the observation estimates obtained using Eq. (2) (dashed curve) for the geopotential at 500 mb, as a function of the iteration number. The rms errors obtained after just four iterations followed by a further iteration with a reduced length scale are indicated by the "X".

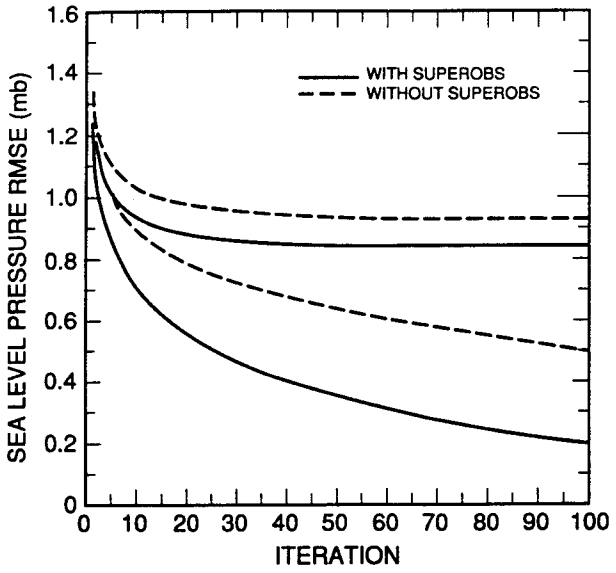

FIG. 8. As in Fig. 7 but for the rms errors of sea level pressure for the case with superobs (solid curve) and without superobs (dashed curve).

In Fig. 8, we illustrate the influence that using superobs has on the rate of convergence of the scheme for the sea level pressure data. The figure compares the rms errors for the analyzed values and the observation estimates of the sea level pressure at the data locations, for cases when superobs are used (solid curve) and when they are not used (dashed curve). Without the superobs, the rate of convergence of the observation estimate is much slower due to the many closely spaced observations (see Bratseth 1986). Even with the superobs, however, the resulting optimum analyses of the sea level pressure (produced after 100 iterations) differ from each other by only 10% in the rms error.

4. Results

The analyses with the new scheme of the cold-air damming, coastal front, subsequent capture of a weak coastal low by a jet streak and the cyclogenesis offshore are described. The results are compared with the enhanced NMC analyses produced with our old Barnes scheme in section 3a. Mesoscale features produced in the new scheme are compared with those described by Bosart's (1988) detailed hand analyses and by Doyle and Warner (1990). Application of the vertical-mode initialization scheme on both the enhanced NMC analyses and our new analyses is used to compare the mesoscale vertical motions and ageostrophic wind derived for each case.

a. Cold-air damming and coastal front

The final 1000-mb analysis produced with the new scheme of the cold-air damming and coastal frontogenesis at 1200 UTC 25 January is shown in Fig. 9a. The analysis has retained the cold-air damming and the temperature contrast along the East Coast, which was produced by the model forecast. In fact, the differences between this 1000-mb analysis in Fig. 9a and that using the Barnes scheme shown in Fig. 4a are small. However, the temperature gradient across the cold front south of the low center over Lake Superior is somewhat stronger with the new analysis. In the new 500-mb analysis shown in Fig. 9b, both the long-wave trough and the cutoff low of 5625 m are in close agreement with the enhanced NMC analysis shown in Fig. 2b. However, as shown in the preceding section, the cutoff low produced with the Barnes scheme in Fig. 4b was much weaker. The −30°C isotherm in the new analysis is east of Lake Superior in agreement with the enhanced NMC analysis in Fig. 2b, whereas the Barnes analysis in Fig. 4b has it lagging to the west around Lake Superior. A jet streak can be seen at 250 mb in

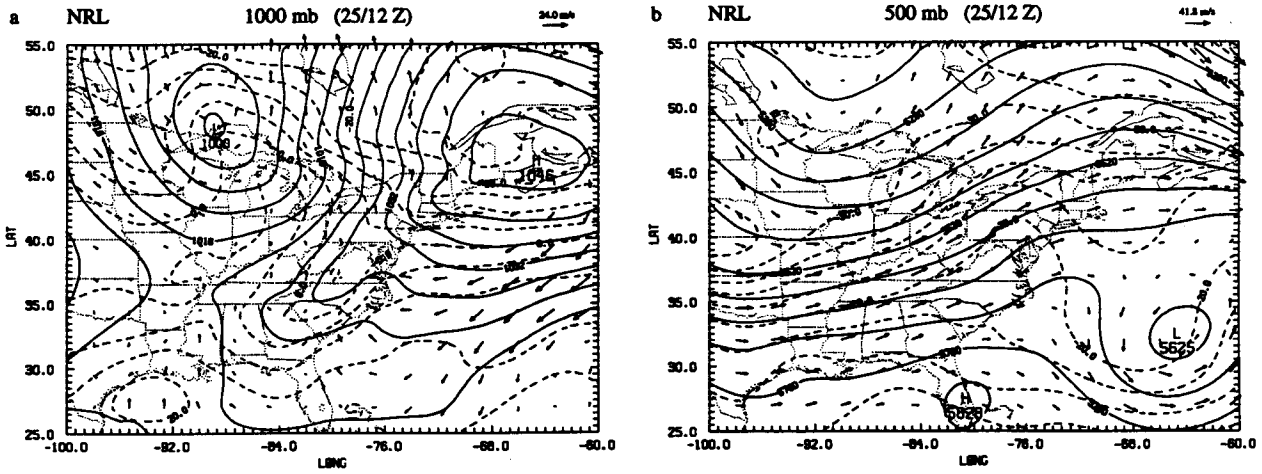

FIG. 9. The NRL analysis for 1200 UTC 25 January of (a) sea level pressure (mb), 1000-mb temperature (°C), and winds, and of (b) the geopotential height (gpm), temperature (°C), and winds at 500 mb. Contours as in Fig. 2.

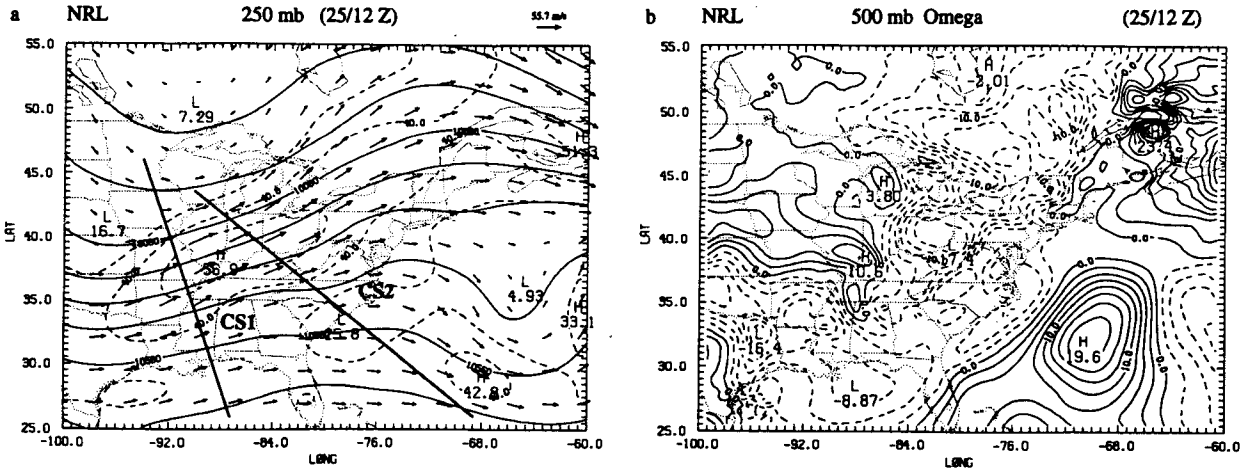

FIG. 10. The NRL analysis for 1200 UTC 25 January of (a) the geopotential height (gpm), temperature (°C), and winds at 250 mb, and of (b) the vertical velocity (mb h^{-1}) at 500 mb. Contours of geopotential are every 120 gpm, and isotachs above 30 m s^{-1} are shown every 10 m s^{-1}. Vertical motion of magnitudes 20 mb h^{-1} or less are contoured every 2.5 mb h^{-1}.

Fig. 10a on the east side of the long-wave trough in the polar jet stream. The subtropical jet stream lies farther to the south across Florida and south of the cutoff low.

The field of vertical motion at 500 mb, which has been derived from the NRL analysis by application of the vertical-mode initialization procedure, is shown in Fig. 10b. Strong ascent from Ohio northeastward on the east side of the long-wave trough and strong subsidence west of the cutoff low are found in close agreement with that that can be derived from the enhanced NMC analysis (not shown). However, the major difference is that the rising motion associated with the developing coastal front along the Carolina coast in the first-guess field is also retained in the NRL analysis. Also two separate centers of rising motion, associated with the surface cyclone located on the southeast Texas coast and the secondary circulation of the upper-level jet's entrance region, are evident over eastern Texas and northern Mississippi. In contrast, only a broad region of ascent can be derived from the enhanced NMC analysis.

To further show the secondary circulations associated with the entrance region of the upper-level jet and the coastal front, cross sections were produced using the initialized fields derived from the new NRL analysis at 1200 UTC 25 January. The locations of the

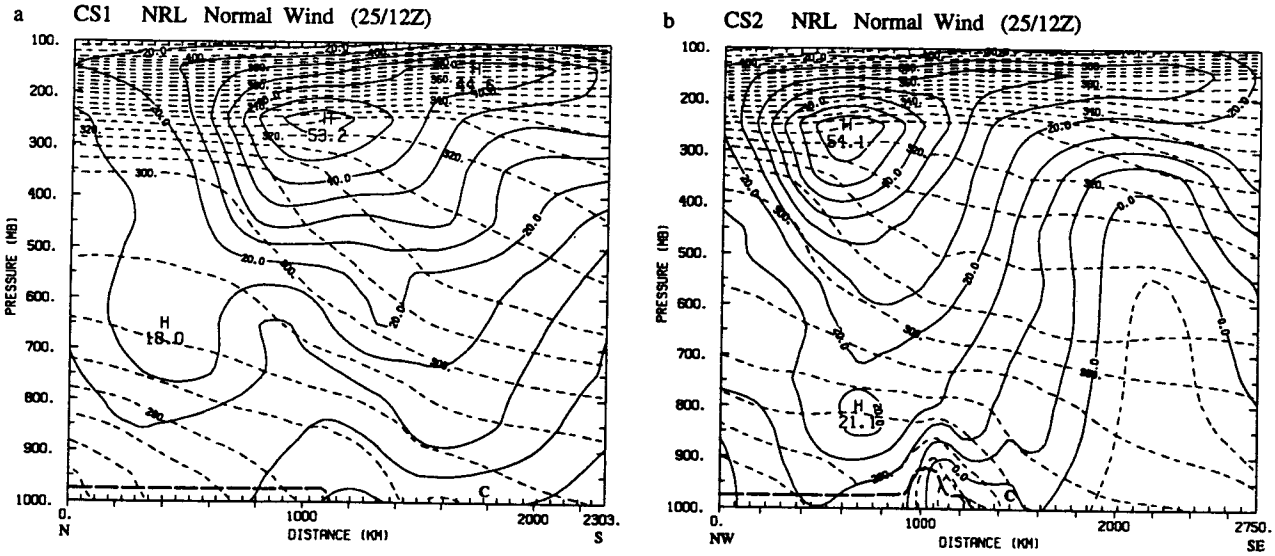

FIG. 11. The wind normal to the plane of the cross sections (a) CS1 from 46°N, 94°W to 26°N, 87.3°W and (b) CS2 from 43.5°N, 90°W to 26°N, 68.7°W for the NRL analysis at 1200 UTC 25 January. Contours every 5 m s^{-1}. The potential temperature (K) is also shown by the dashed contours every 5 K in the troposphere. The position of the model grid points every 0.5° in latitude are shown by the inner tick marks, and coastline by the "C."

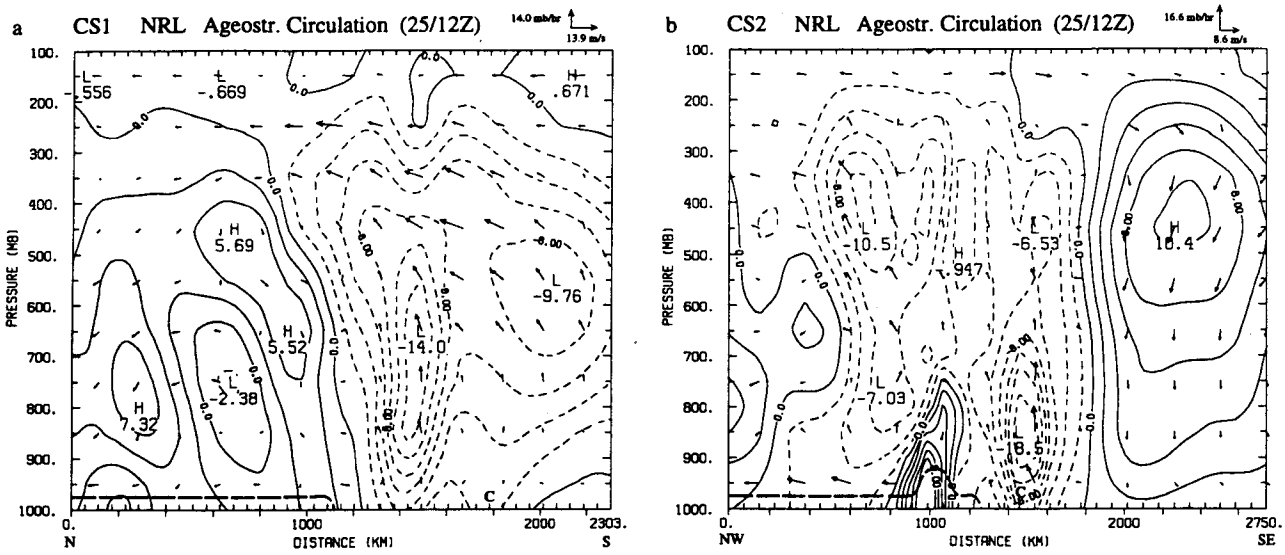

FIG. 12. As in Fig. 11 but for the vertical motion and ageostrophic wind in the plane of the cross sections (a) CS1 and (b) CS2. Contours of the vertical motion are every 2 mb h^{-1}. Scale of vectors indicated by labeled arrows.

two cross sections are displayed in Fig. 10a. Cross section CS1, which extends from Minnesota to the central Gulf of Mexico, cuts across the entrance region of the upper-level polar jet. In Fig. 11a, the wind speed normal to cross section CS1 shows the core of the polar jet at 250 mb and the subtropical jet lying farther to the south at 150 mb. A narrow region of ascending motion with a maximum ascent of 14 mb h^{-1} can be seen in Fig. 12a over northern Mississippi in the right rear flank of this polar jet. Aloft, a strong southerly ageostrophic flow across the jet is followed by weaker subsidence to the north. Such a thermally direct circulation in the rear of the jet streak is well known (e.g., Uccellini and Johnson 1979; Keyser and Shapiro 1986). Weaker ascent associated with the subtropical jet stream to the south is also evident in the figure. In comparison, the secondary circulation produced by the enhanced NMC analysis has a broader region of ascending motion in the rear of the polar jet streak (Fig. 13a). The second cross section CS2, which is perpendicular to the Carolina coast, cuts across the region of the coastal front and through the polar jet aloft. The cold air trapped between the coast and the Appalachians can be seen in Fig. 11b, with the jet core aloft to the northwest. The low-level jet west of the Appalachians in the figure provides the inflow to the low pressure system over

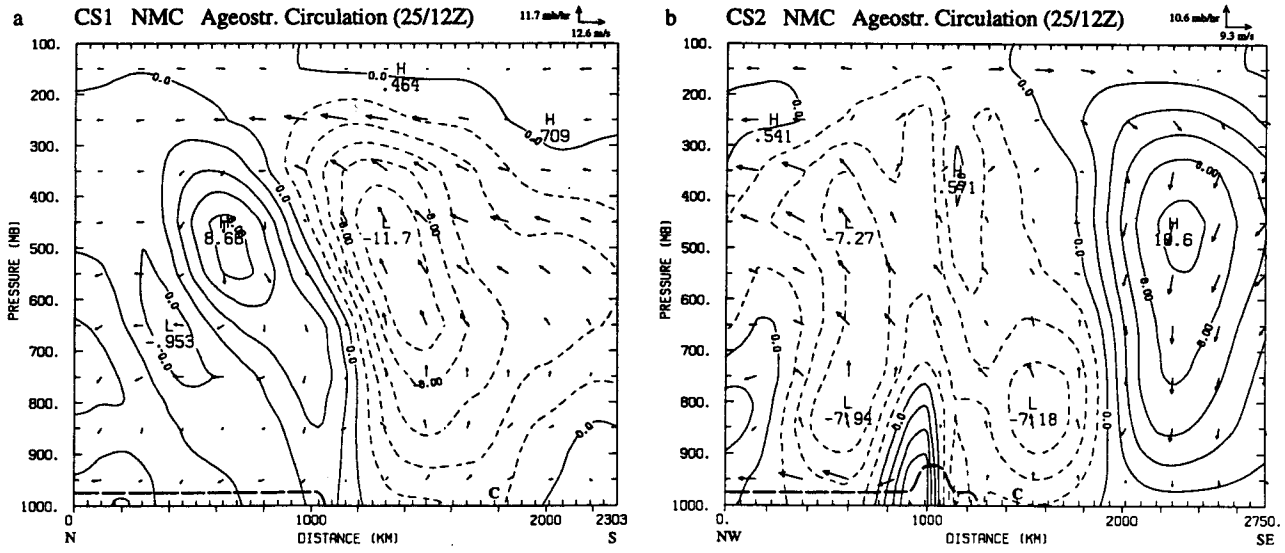

FIG. 13. The vertical motion and ageostrophic wind in the plane of the cross sections (a) CS1 and (b) CS2 for the enhanced NMC analysis. Contours as in Fig. 12.

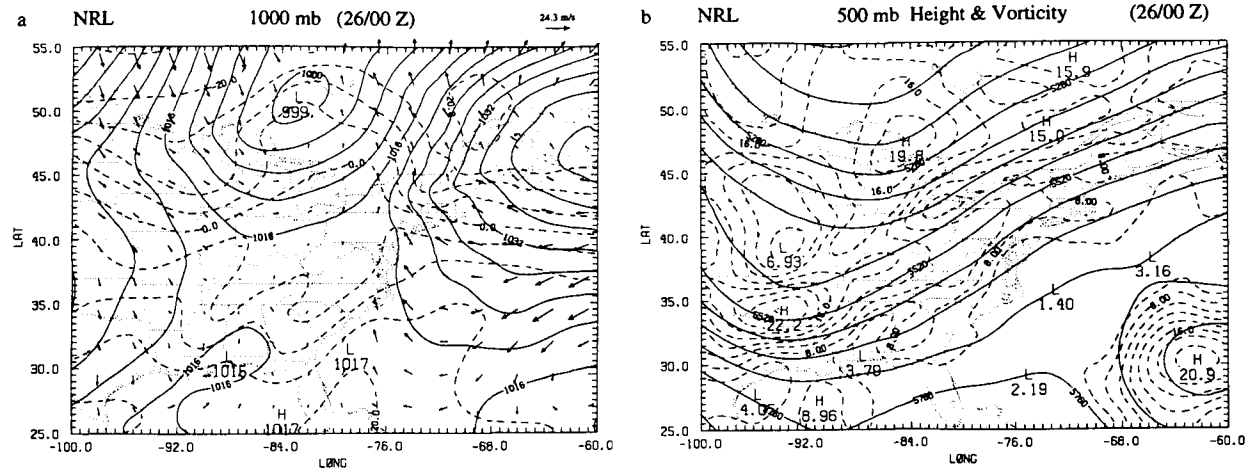

FIG. 14. The NRL analysis for 0000 UTC 26 January of (a) sea level pressure (mb), 1000-mb temperature (°C), and winds; and of (b) the geopotential height (gpm), absolute vorticity ($\times 10^{-5}$ s^{-1}) at 500 mb. Contours of vorticity are every 2×10^{-5} s^{-1} for values above 6×10^{-5} s^{-1}.

Lake Superior (Fig. 9a). In Fig. 12b, shallow ascent with maximum of 18.5 mb h^{-1}, which is associated with the coastal front generated in the first-guess forecast, can be seen in a narrow band at the coastline. This ascent is in good agreement with that shown by Doyle and Warner (1990) in their cross section normal to the coastal front (see their Fig. 15). The subsidence west of the cutoff low in the subtropical jet stream and ascent east of the approaching upper-level trough can also seen in Fig. 12b. The coastal front circulation is much stronger and more well defined with the new analysis than the circulation shown in Fig. 13b, which is derived from the enhanced NMC analysis.

b. *Interaction of jet streak with coastal front*

By 0000 UTC January 26, the coastal front had developed from Georgia to southern New England in an onshore easterly flow regime and led to the erosion of the cold dome east of the Appalachians (Doyle and Warner 1990). The strong thermal gradient associated with the coastal front is seen along the coast of the Carolinas in the NRL 1000-mb analysis illustrated in Fig. 14a. In this case, the NRL analysis was able to significantly sharpen the temperature contrast between the Carolina coast and the Appalachians compared to that which was produced by the first-guess forecast (see

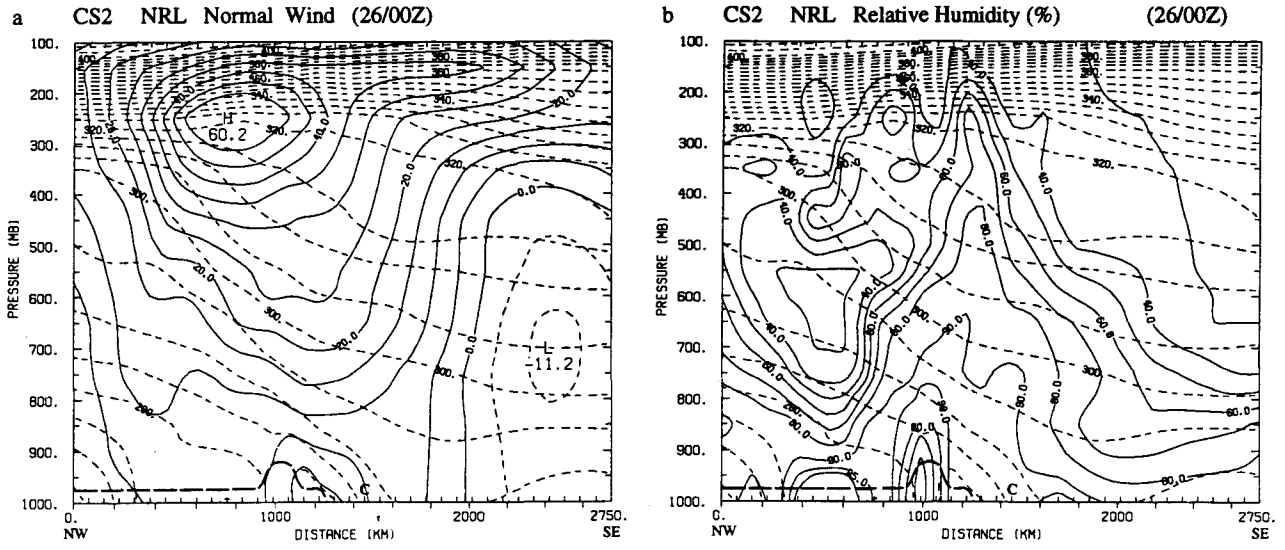

FIG. 15. (a) The wind normal to the plane of cross section CS2 and (b) the relative humidity (%) in the plane of the same cross section for the NRL analysis at 0000 UTC 26 January. Contours as in Fig. 11.

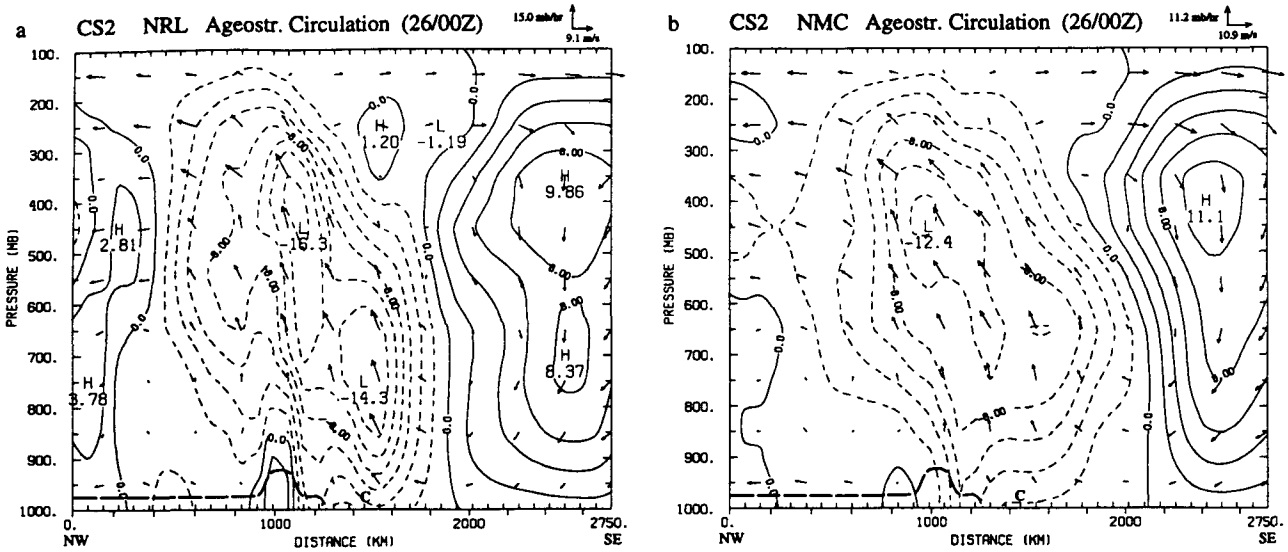

FIG. 16. The vertical motion and ageostrophic wind in the plane of cross section CS2 at 0000 UTC 26 January for (a) the NRL analysis and for (b) the enhanced NMC analysis. Contours as in Fig. 12.

Harms et al. 1992). The weak coastal low, which developed at the southern end of the coastal front (Bosart 1988; Doyle and Warner 1990), is also indicated in our analysis. The surface low associated with the a major short wave can be seen along the Alabama coast. This short wave can be seen as a strong vorticity maximum at the base of the long-wave trough at 500 mb in Fig. 14b. The polar jet across the eastern United States is strengthening as the short wave over the Great Lakes is moving eastward, producing a confluent flow into the jet. A weaker vorticity maximum can be seen over Georgia in the region of the interaction of the secondary circulation in the entrance region of the strengthening jet with the weak low on the coastal front.

This interaction of the secondary circulation in the entrance region of the jet with the weak coastal low at the southern end of the coastal front can be seen in the cross section CS2 across the coast shown in Figs. 15 and 16. Figure 15a shows the strengthening winds in the jet at 250 mb, while the ageostrophic flow and vertical motion are shown in Fig. 16a. A deep circulation can be seen linking the coastal low with the easterly ageostrophic flow across the upper-level jet. A further component of the circulation is linked to the subsidence west of the cutoff low in the subtropical jet stream to the southeast. Much weaker ascent is found in the lower troposphere when using the enhanced NMC analysis to derive the circulation (Fig. 16b). High

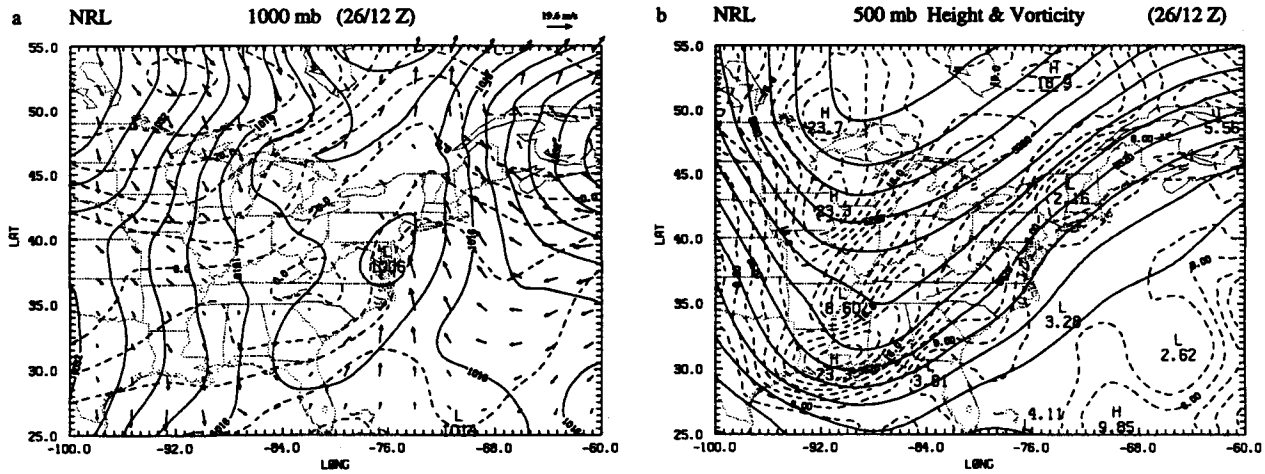

FIG. 17. The NRL analysis for 1200 UTC 26 January of (a) sea level pressure (mb), 1000-mb temperature (°C), and winds, and (b) the geopotential height (gpm), absolute vorticity ($\times 10^{-5}$ s^{-1}) at 500 mb. Contours as in Fig. 14.

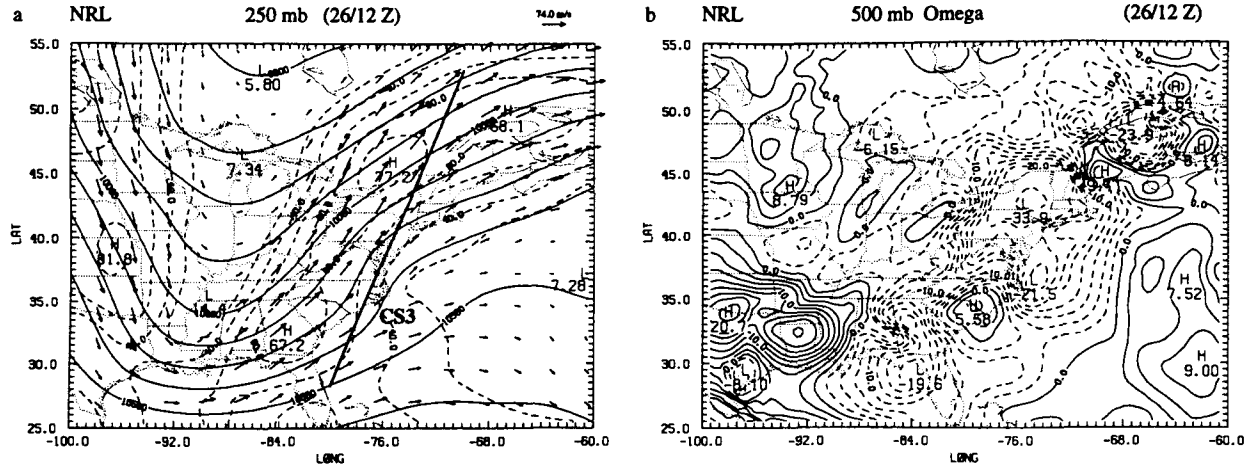

FIG. 18. (a) The geopotential height (gpm), temperature (°C), and winds at 250 mb; and (b) the vertical velocity (mb h^{-1}) at 500 mb for the NRL analysis at 1200 UTC 26 January. Contours as in Fig. 10.

humidities of greater than 90% are analyzed in Fig. 15b over the coastal front, consistent with developing precipitation observed in the region (Doyle and Warner 1990).

c. *Cyclogenesis offshore*

The 1000-mb analysis for 1200 UTC 26 January in Fig. 17a shows the coastal low has moved north to the Chesapeake Bay and is merging with a large region of weak low pressure over the northeast. Over the Great Lakes, a secondary wave is developing along a strong front. The surface pressure is falling over the southeast as the strong southern short wave aloft can be seen reaching the base of the long-wave trough in Fig. 17b. The short wave from the Great Lakes has merged with the northern jet as it moved northeastward, contributing to stronger vorticity gradients over the St. Lawrence River in the right rear flank of the jet. The weak vorticity maximum from Georgia (Fig. 14b) has moved northeastward to southwest Virginia in Fig. 17b, with the coastal low moving ahead of it. Figure 18a shows the northern jet approaching the top of the ridge and the southern jet at the base of the long-wave trough at 250 mb. At 500 mb, two strong centers of ascent can be seen to have developed in Fig. 18b over New York State below the right rear flank of the northern jet, as it strengthened, and off Cape Hatteras to the southeast

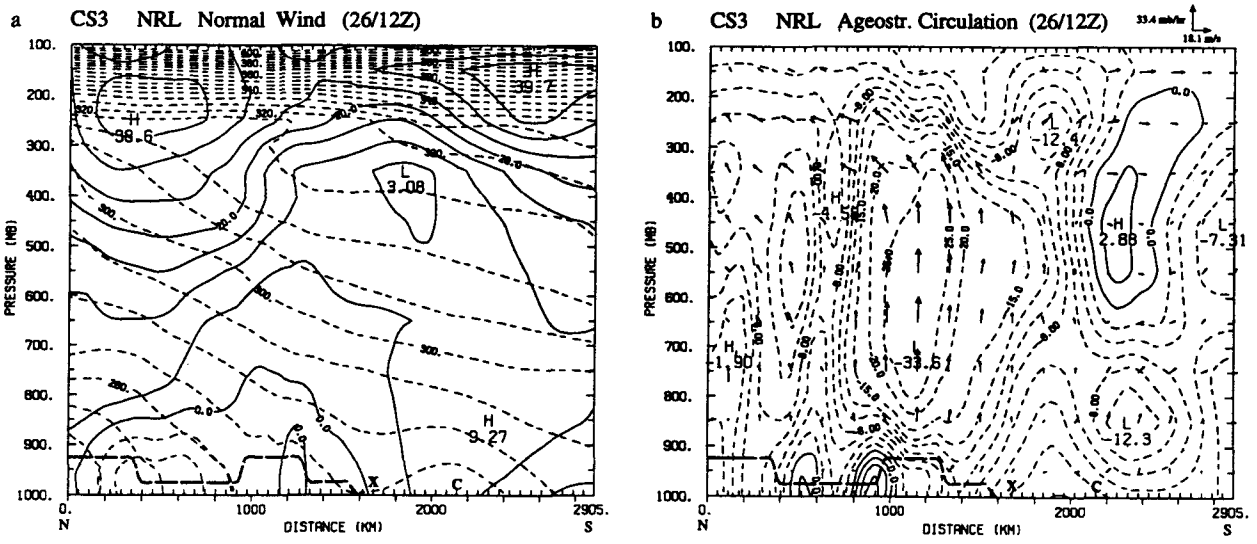

FIG. 19. (a) The wind normal to the cross section CS3 from 53°N, 70°W to 28°N, 80°W and (b) the vertical motion (mb h^{-1}) and ageostrophic wind (m s^{-1}) in the plane of cross section for 1200 UTC 26 January. Contours as in Figs. 11 and 12 except that contours of vertical motion less than −12 and −40 mb h^{-1} are every 5 and 15 mb h^{-1}, respectively.

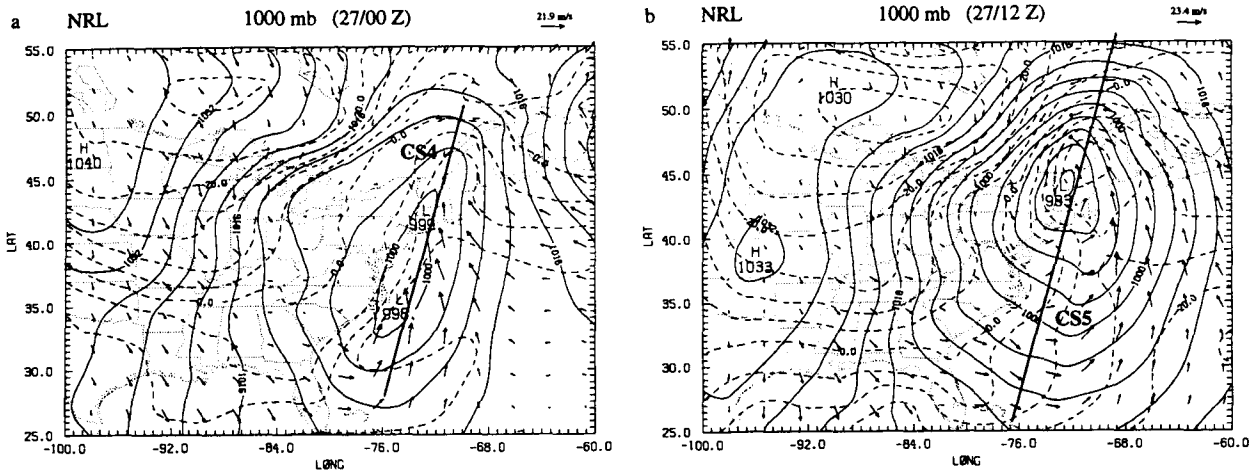

FIG. 20. The sea level pressure (mb), 1000-mb temperature (°C), and winds for the NRL analysis at (a) 0000 UTC and (b) 1200 UTC on 27 January. Contours as in Fig. 2.

of the center of the coastal low as it moved with the jet. The region of ascent over Florida is in response to the exit region of the southern jet at the base of the long-wave trough.

The merging of the circulations associated with the entrance region of the northern jet and the coastal low are illustrated in a cross section CS3 along the coastline cutting through the northern jet and coastal low (see Fig. 18a). The northern jet at 250 mb and the subtropical jet stream to the south at 150 mb can be seen in the wind normal to the cross section in Fig. 19a. The corresponding ageostrophic circulation in the plane of the cross section is shown in Fig. 19b. A strengthened direct secondary circulation in the entrance region of the northern jet can be seen with maximum ascent of 33.6 mb h^{-1} and southerly ageostrophic flow aloft to the north. The northerly ageostrophic flow to the south in the upper troposphere is associated with the subtropical jet stream. The position of the coastal low is shown by the "X" to the rear of the region of strongest ascent in the northern jet's secondary circulation. Ascent at the southern end of the cross section is associated with the exit region of the approaching jet at the base of the long-wave trough.

The 1000-mb analyses for 0000 and 1200 UTC 27 January are shown in Figs. 20a and 20b. They show the development of a new low off Cape Hatteras, which moves northward and deepens rapidly to overshadow the earlier coastal low. Cross sections CS4 and CS5 are taken along the coast to show the evolution of the secondary circulations associated with the two jets during this period. The positions of the jets for each cross section can be seen in Figs. 21a and 21c, and the corresponding ageostrophic circulations in Figs. 21b and 21d. The positions of the lows are indicated by the "X" in the figures. As the southern jet rounds the long-wave trough and crosses the coast at 0000 UTC, the new low can be seen developing beneath strong ascent and northerly ageostrophic flow aloft in the exit region of this jet (Fig. 21b). The circulation associated with the northern jet and surface low is a separate circulation to the north at this stage. The rapid development of the new low in the next 12 h can be seen in Figs. 21c and 21d to be associated with the movement of the southern jet and its secondary circulation northward. By 1200 UTC, this secondary circulation in the southern jet has caught up with the circulation in the entrance region of the northern jet, so that they cooperate in strengthening the ascent in the rapidly developing low. Such cooperation has been found in other cases analyzed by Uccellini and Kocin (1987).

5. Summary and conclusions

During the last decade optimal interpolation replaced successive correction methods as the dominant objective analysis technique in operational weather forecasting systems. However, with the advent of Bratseth's (1986) analysis scheme, which converges to the optimal interpolation solution, the less expensive approach of successive correction has become a powerful and attractive alternative analysis method. The objective analysis scheme developed for use with the NRL limited-area weather prediction model uses the Bratseth scheme, in which the data weights are dependent on the covariance between observations, are reduced in regions of higher data density, and include observational errors. We have devised a computationally inexpensive method for linking the mass and momentum fields that is different from earlier methods reported in the literature (e.g., Cressman 1959; Lorenc et al. 1991). The key element is obtaining the gradient of the geopotential change from the change in an estimated geostrophic wind at each iteration to enhance the initial

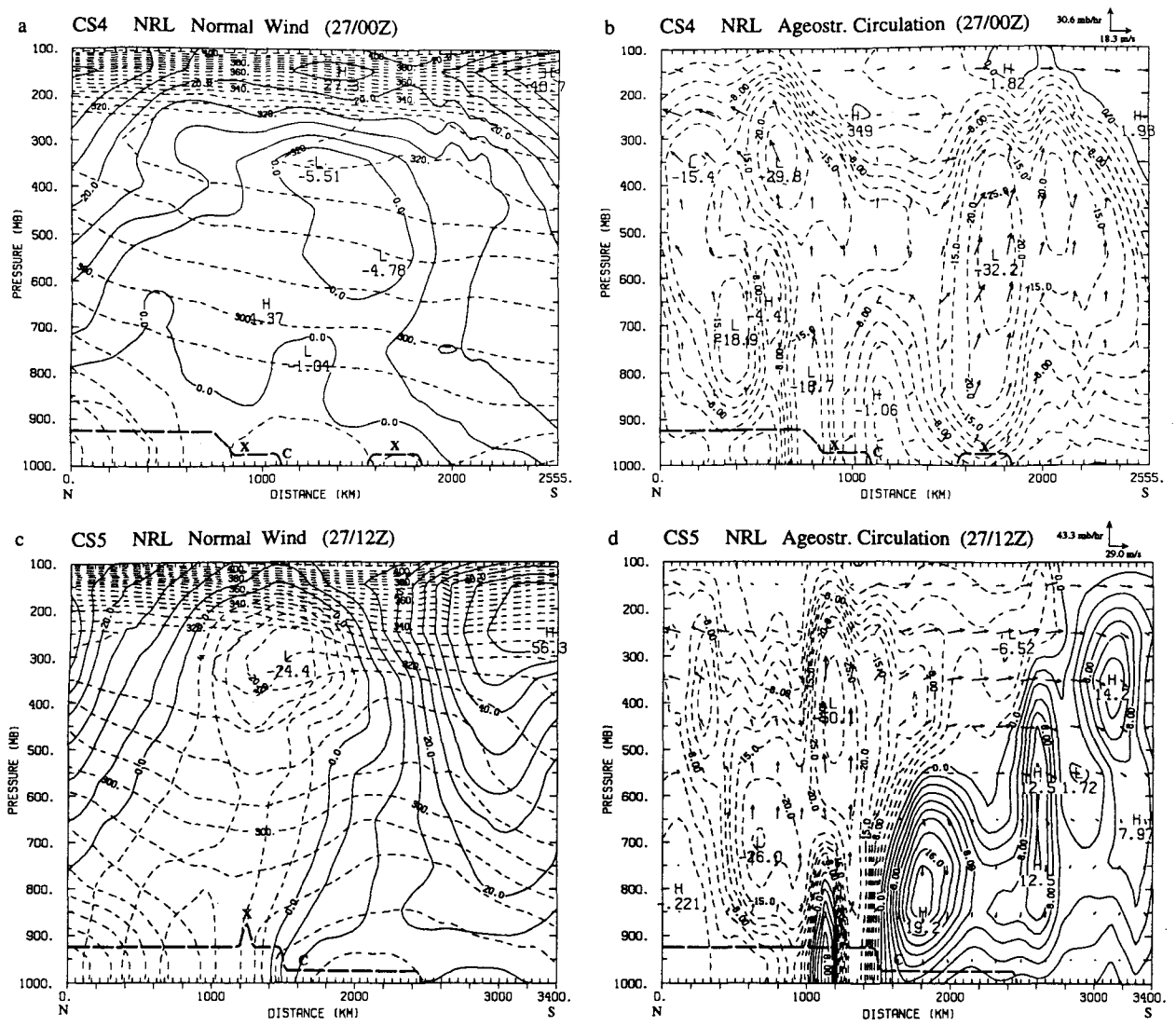

FIG. 21. (a) The wind normal to a cross section CS4 from 50.5°N, 70°W to 28°N, 76°W and (b) the vertical motion (mb h^{-1}) and ageostrophic wind (m s^{-1}) in the plane of cross section CS4 for the NRL analysis at 0000 UTC 27 January. Here (c) and (d) are the same as (a) and (b) but for cross section CS5 from 55.5°N, 68.7°W to 25.5°N, 76.7°W at 1200 UTC 27 January. Contours as in Fig. 19.

univariate analysis of the geopotential. We use the initial univariate wind analysis to provide only the starting estimate of the geostrophic wind for the first iteration. For subsequent iterations, the geostrophic wind is estimated from the updated geopotential gradient. After this enhancement of the geopotential, the univariate wind analysis is updated for the change in the geostrophic wind.

An evaluation of the NRL objective analysis scheme has been accomplished using a GALE IOP 2 dataset. The use of a prior model forecast as a first guess for the analysis was crucial in obtaining mesoscale features in the analysis. Such features were not produced by our earlier scheme, which used a Barnes (1973) scheme to enhance NMC hemispheric analyses (Chang et al. 1989; Shi et al. 1991). Over the region of the eastern United States, where there is a large amount of data, the Barnes scheme produced as good an analysis as the Bratseth (1986) scheme, when the same first-guess forecast is used. The Bratseth scheme was more superior in the other regions where it could adjust for the changing data density. Our simple geostrophic method for linking the mass and wind-field analyses provided tighter gradients in these fields, particularly in the regions of lower data density outside of the eastern United States.

For the second IOP of GALE, the vertical circulations were derived from the analyses by application of the vertical-mode initialization scheme of Bourke and McGregor (1983). Superior mesoscale vertical circulations were produced in the coastal low and upper-tropospheric jet streaks with the new NRL analysis

scheme when compared to that derived from the earlier Barnes enhancement of the NMC hemispheric analyses. These circulations clearly demonstrated the interaction of the coastal low with the entrance region of a jet streak in the upper troposphere. The cooperation of the secondary circulations in two jets during offshore cyclogenesis is also shown. Being able to produce such mesoscale circulations using these analysis and initialization schemes is important for providing accurate initial conditions for generating forecasts with the limited-area model. Future work will use these improved analyses with the initialization scheme to test assimilating the GALE data in a limited-area analysis–forecast system.

Acknowledgments. This research was sponsored by NRL's basic research program and by SPAWAR of the U.S. Navy. The first author was supported at Science Applications International Corporation under Contract N00014-89-R-HB08 with NRL, and the second author was supported as a graduate student at North Carolina State University by the U.S. Air Force. Part of the computer time was provided by the North Carolina Super Computing Center, Research Triangle Park.

REFERENCES

Barnes, S. L., 1973: Mesoscale objective map analysis using weighted time-series observations. NOAA Tech. Memo., ERL NSSL-62, Norman, OK, 60 pp.

Benjamin, S. G., 1989: An isentropic meso-scale analysis system and its sensitivity to aircraft and surface observations. *Mon. Wea. Rev.*, **117**, 1586–1603.

——, and N. L. Seaman, 1985: A simple scheme for objective analysis in curved flow. *Mon. Wea. Rev.*, **113**, 1184–1198.

Bergthórsson, P., and B. R. Döös, 1955: Numerical weather map analysis. *Tellus*, **7**, 329–340.

Bosart, L. F., 1988: Coastal frontogenesis and cyclogenesis during GALE IOP #2. Preliminary Reports, GALE/CASP Workshop, Virginia Beach, VA, NCAR 75-93. [Available from GALE Project Office, P.O. Box 3000, Boulder CO 80807.]

Bourke, W., and J. L. McGregor, 1983: A nonlinear vertical mode initialization scheme for a limited area prediction model. *Mon. Wea. Rev.*, **111**, 2285–2297.

Bratseth, A. M., 1986: Statistical interpolation by means of successive corrections. *Tellus*, **38A**, 439–447.

Chang, S., K. Brehme, R. Madala, and K. Sashegyi, 1989: A numerical study of the East Coast snow storm of 10–12 February 1983. *Mon. Wea. Rev.*, **117**, 1768–1778.

Cressman, G., 1959: An operational objective analysis system. *Mon. Wea. Rev.*, **87**, 367–374.

DiMego, G. J., 1988: The National Meteorological Center regional analysis system. *Mon. Wea. Rev.*, **116**, 977–1000.

Dirks, R. A., J. P. Kuettner, and J. A. Moore, 1988: Genesis of Atlantic Lows Experiment (GALE): An overview. *Bull. Amer. Meteor. Soc.*, **69**, 148–160.

Doyle, J. D., and T. T. Warner, 1990: Mesoscale coastal processes during GALE IOP 2. *Mon. Wea. Rev.*, **118**, 283–308.

Grønås, S., and K. H. Midtbø, 1987: Operational multivariate analyses by successive corrections. Collection of papers presented at WMO/IUGG numerical weather prediction symposium, Tokyo, 4–8 August 1986. *J. Meteor. Soc. Japan*, 61–74.

Harms, D. E., K. D. Sashegyi, R. V. Madala, and S. Raman, 1992: Four-dimensional data assimilation of GALE data using a multivariate analysis scheme and a mesoscale model with diabatic initialization. NRL Tech. Memo. Rep., No. 7147, Naval Research Laboratory, Washington D.C., 236 pp. [NTIS A256063.]

Hollingsworth, A., and P. Lönnberg, 1986: The statistical structure of short-range forecast errors as determined from radiosonde data. Part I: The wind field. *Tellus*, **38A**, 111–136.

Keyser, D., and M. A. Shapiro, 1986: A review of the structure and dynamics of upper-level frontal zones. *Mon. Wea. Rev.*, **114**, 452–499.

Kistler, R. E., and R. D. McPherson, 1975: On the use of a local wind correction technique in four-dimensional data assimilation. *Mon. Wea. Rev.*, **103**, 445–449.

Koch, S. E., M. DesJardins, and P. J. Kocin, 1983: An interactive Barnes objective map analysis scheme for use with satellite and conventional data. *J. Climate Appl. Meteor.*, **22**, 1487–1503.

Lorenc, A. C., R. S. Bell, and B. MacPherson, 1991: The Meteorological Office analysis correction data assimilation scheme. *Quart. J. Roy. Meteor. Soc.*, **117**, 59–89.

Madala, R. V., S. W. Chang, U. C. Mohanty, S. C. Madan, R. K. Paliwal, V. B. Sarin, T. Holt, and S. Raman, 1987: Description of the Naval Research Laboratory Limited Area Dynamical Weather Prediction Model. NRL Tech. Memo. Rep., No. 5992, Naval Research Laboratory, Washington, D.C., 131 pp. [NTIS A182780.]

Mills, G. A., and R. S. Seaman, 1990: The BMRC regional data assimilation system. *Mon. Wea. Rev.*, **118**, 1217–1237.

Mercer, T. J., 1987: *Genesis of Atlantic Lows Experiment (GALE): Data Users Guide.* GALE Data Center, Department of Physics and Atmospheric Science, Drexel University, 106 pp.

Raman, S., and A. J. Riordan, 1988: Genesis of Atlantic Lows Experiment: The planetary-boundary-layer subprogram of GALE. *Bull. Amer. Meteor. Soc.*, **69**, 161–172.

Reynolds, R. W., 1982: A monthly averaged climatology of sea surface temperatures. NOAA Tech. Rep., NWS-31, Climate Analysis Center, National Weather Service, Washington, D.C., 35 pp.

Riordan, A. J., 1990: Examination of the mesoscale features of the GALE coastal front of 24–25 January 1986. *Mon. Wea. Rev.*, **118**, 258–282.

Sashegyi, K. D., and R. V. Madala, 1990: Tests of initialization procedures with the NRL limited area numerical weather prediction model. NRL Tech. Memo. Rep., No. 6648, Naval Research Laboratory, Washington D.C., 88 pp. [NTIS A223549.]

——, and ——, 1993: Application of vertical mode initialization to a limited area model in flux form. *Mon. Wea. Rev.*, **121**, 207–220.

Schlatter, T. W., 1988: Past and present trends in the objective analysis of meteorological data for nowcasting and numerical forecasting. Preprints, *Eighth Conf. on Numerical Weather Prediction*, Baltimore, MD, Amer. Meteor. Soc., J9–J25.

Seaman, R. S., 1988: Some real data tests of the interpolation accuracy of Bratseth's successive correction method. *Tellus*, **40A**, 173–176.

Shaw, D. B., P. Lönnberg, A. Hollingsworth, and P. Undén, 1987: Data assimilation: The 1984/85 revisions of the ECMWF mass and wind analysis. *Quart. J. Roy. Meteor. Soc.*, **113**, 533–566.

Shi, J. J., S. Chang, K. Sashegyi, and S. Raman, 1991: Enhancement of objective analysis of Hurricane Florence (1988) with dropsonde data. Preprints, *19th Conf. on Hurricanes and Tropical Meteorology*, Miami, Amer. Meteor. Soc., 335–337.

Uccellini, L. W., and D. R. Johnson, 1979: The coupling of lower tropospheric jet streak and implications for the development of severe convective storms. *Mon. Wea. Rev.*, **107**, 682–703.

——, and P. J. Kocin, 1987: The interaction of jet streak circulations during heavy snow events along the east coast of the United States. *Wea. Forecasting*, **2**, 289–308.

——, ——, R. A. Petersen, C. H. Wash, and K. F. Brill, 1984: The Presidents' Day cyclone of 18–19 February 1979: Synoptic overview and analysis of the subtropical jet streak influencing the pre-cyclogenetic period. *Mon. Wea. Rev.*, **112**, 31–55.

Warner, T. T., M. N. Lakhtakia, J. D. Doyle, and R. A. Pearson, 1990: Marine atmospheric boundary layer circulations forced by Gulf Stream sea surface temperature gradients. *Mon. Wea. Rev.*, **118**, 309–323.